Simulation Studies of Peptide Aggregation

by

Michael McGovern

A dissertation submitted in partial fulfillment of the requirements for the degree of

Doctor of Philosophy (Chemical Engineering)

at the

UNIVERSITY OF WISCONSIN-MADISON

2014

Date of Final Oral Examination: 5/21/14

The dissertation is approved by the following members of the Final Oral Committee

Juan de Pablo, Professor, Chemical Engineering
Nicholas Abbott, Professor, Chemical Engineering
Sean Palecek, Professor, Chemical Engineering
Eric Shusta, Professor, Chemical Engineering
Qiang Cui, Professor, Chemistry

Acknowledgements

I would like to thank a few of the people who made this thesis possible. First of all, I owe a debt of gratitude to professor Juan de Pablo, whose advice, patience, and support were indispensible to me. I especially appreciated his calm, reasonable advice when things went wrong, and I have learned from it.

When I started doing research, it was Dr. Clark Miller and Dr. Santosh Reddy who taught me the basics about the tools I would be using, and I am very grateful to them for being so willing to answer all of my questions. I enjoyed collaborating with Dr. Aslin Izmitli, who carried out the experimental work presented here. Kyle Hoffmann has been very helpful to me on many occasions with his great amount of knowledge, and I was lucky to work with him on his force field validation project. I am thankful to everyone in the de Pablo group who offered me help over the years, especially Lucas Antony, Dr. Chi-cheng Chui, Sadanand Singh, and Aaron Fluitt. I would also like to acknowledge James Dama of the University of Chicago, for helpful conversations about my research on metadynamics.

Finally I would like to thank my family and especially my parents for their support.

Table of Contents

Acknowledgements i

List of Figures iv

Abstract vii

Chapter 1: Introduction 1

1.1 References 3

Chapter 2: A Boundary Correction Algorithm for Metadynamics in Multiple Dimensions 5

2.1 Introduction 5

2.2 Methods 8

2.3 Model Systems 11

2.4 Conclusion 16

2.5 References 17

Chapter 3: Dimerization of Helical Beta-Peptides in Solution 18

3.1 Introduction 18

3.2 Materials and Methods 24

3.3 Results and Discussion 27

3.4 Comparison of Metadynamics and Constraint Force Methods 33

3.5 Conclusions 35

3.6 References 37

Chapter 4: Effect of trehalose on the interaction of human islet amyloid polypeptide with lipid membranes 39

4.1 Introduction 39

4.2 Simulation Methods 41

4.3 Choice of Force Fields 45

4.4 Simulation Details 48

4.6 Discussion 62

4.6 References 64

Conclusions 69

Appendix A1: Experimental Methods for hIAPP System 70

List of Figures

Figure 2-1: Free energy for non-interacting model system. Exact free energy (a) using no boundary correction (b), (different scale from other figures), inversion condition (c), additive algorithm (d), and multiplicative methods from this paper (e). All energy units are kJ/mol. 13

Figure 2-2: Free energy profile for alanine dipeptide model system is, from a simulation with boundary errors corrected over a 125ns molecular dynamics calculation using the bias from the multiplicative algorithm presented here(a). The free energy of the same system using traditional metadynamics with a standard invert condition is shown in (b), while the free energy generated using the multiplicative algorithm presented here is shown in (c). All energy units are kJ/mol. 15

Figure 2-3: Average absolute error as a function of CPU time for the invert condition and multiplicative correction in the free energy minimum corner (defined as cos(φ)<-0.75, cos(ψ)<-0.75). Both systems were simulated for 4ns of simulation time, with the multiplicative method system taking 650s of CPU time, and the invert condition system taking 1000s of CPU time. 16

Figure 3-1: A 14-helical β-peptide. The residues are colored as follows: Red - β^3-hTyr ; Green – ACHC; Blue - β^3-hLys ; Yellow - β^3-hPhe 19

Figure 3-2: Illustration of the four peptides studied showing globally amphiphilic and non-globally amphiphilic display of hydrophobic and hydrophilic groups 20

Figure 3-3: Structures of the four β-peptides 21

Figure 3-4: Illustration of the definition of the helix angle. In this figure peptide 1a is represented schematically. Here the two peptides align with their end-to-end vectors parallel. A vector is defined between two fixed atoms on the helix backbone for each peptide (the α-carbon of the fifth residue and the β-carbon of the sixth residue). In this case the angle is near 180°.Figure 5: Free energy surface for peptide 1a as a function of distance and helix angle in units of kJ/mol. Two deep free energy minima appear. They each correspond to the peptides aligning with hydrophobic faces pointing towards each other, with the end-to-end vectors nearly parallel in one case, and nearly anti-parallel in the other. 27

Figure 3-5: Free energy surface for peptide 1a as a function of distance and helix angle in units of kJ/mol for a cubic simulation box of 5.4nm(a) and 6nm(b). There are two deep free energy minima at a separation of around 0.7nm, one with a high helix angle corresponding to a parallel configuration of the end-to-end vectors and one with a low helix angle corresponding to anti-parallel end-to-end vectors. No finite size effects are apparent. 28

Figure 3-6: Free energy surface for peptide 1b as a function of distance and helix angle in units of kJ/mol. There is only a single shallow minimum in the free energy. 29

Figure 3-7: Representative configuration of the free energy minimum structure for peptide 1a with the hydrophobic groups facing each other and the end-to-end vectors nearly parallel 30

Figure 3-8: Free energy surface for peptide 2a as a function of distance and helix angle in units of kJ/mol. Here the preference for helix angles near 0° or 180° is greatly reduced compared to peptide 1a. 31

Figure 3-9: Free energy surface for peptide 2b as a function of distance and helix angle in units of kJ/mol. The free energy minimum is significantly deeper than in the case of peptide 1b, and the angular preference is strong. 32
Figure 3-10: Typical frame of the free energy minimum configuration of peptide 2b (right) shown from two angles. 33
Figure 3-11: Distance and helix angle tracked over 40ns of a metadynamics calculation 34
Figure 3-12: Helix angle as a function of time for a 20 ns constraint force simulation 35
Figure 4-1: System to be simulated with explicit solvent not shown for clarity 42
Figure 4-2: Examples of distinct conformations with zero α-helix content 44
Figure 4-3: Free energy surfaces from metadynamics simulations of rIAPP in water as a function of α-helix and β-sheet character. The force fields are, clockwise from the top left: OPLS, GROMOS53a6, CHARMM22*, Amber99sb*ILDN, Amberff03w, and CHARMM27 46
Figure 4-4: Comparison of experimental NMR shift data to predictions from simulations for CHARMM22, GROMOS53a6 and OPLS 47
Figure 4-5: Comparison of experimental NMR shift data to predictions from simulations for Amber99sb*ILDN, Amberff03w, and CHARMM22* 48
Figure 4-6: Compression isotherms of DPPG on water, 100 mM trehalose, PBS and PBS/100mM trehalose subphases at 30°C. 52
Figure 4-7: -Surface tension vs. area isotherm for hIAPP-DPPG system with and without trehalose 52
Figure 4-8: Percent area change versus time isotherms of a DPPG film at a constant surface pressure of 25 mN/m after injection of hIAPP into the aqueous subphase at time zero. 54
Figure 4-10: Fluorescence micrographs showing the domain morphology of a DPPG monolayer at 30ºC and 25mN/m on (a,b,c) water and (d,e,f) trehalose subphases (a,d) before and (b,e) 30 min after and (c,f) 2 hours after peptide injection into the subphase. The scale bars is 100nm. 56
Figure 4-11: hIAPP fiber formation monitored by Thioflavin T (Th T) fluorescence along time at 30°C. All the samples without liposomes (water, trehalose, PBS, PBS/trehalose) gave similar results for the time range shown in this figure (x). 57
Figure 4-12: Calcein leakage from DPPG large unilamellar vesicles induced by hIAPP. Each experiment was repeated three times; the average and the standard deviation are shown. All experiments were performed in PBS, pH 7.4 at 30°C. 59
Figure 4-13: Secondary structure vs. time for hIAPP in a bulk solution of water(a), 100mM trehalose (b), and 200mM trehalose (c). α-helix is in blue 60
Figure 4-14: hIAPP secondary structure vs. time in the presence of a DPPG monolayer solvated in (a) water and (b) water and trehalose. 61
Figure 4-15: Representative frames from REST simulations of hIAPP in the presence of a DPPG monolayer and solvated in water (left) and water/trehalose (right). 62

Abstract

An improved free energy calculation method for molecular simulations is presented which allows for accurate calculation of free energy as a function of multiple variables simultaneously without the systematic boundary errors that have plagued similar methods in the past. Molecular simulations are applied to study the aggregation behavior of β-peptides, a class of synthetic protein-like molecules in order to learn about how molecular level properties lead to large scale self-assembly properties. Finally, simulations are used to examine the structure of human islet amyloid polypeptide, a peptide hormone whose aggregation is associated with diabetes, in a variety of experimental conditions in order to learn about how the solvent environment effects aggregation

Chapter 1: Introduction

Methods to accurately calculate free energies are essential for many applications of molecular simulations. By predicting not only the most preferred states, but also the relative statistical weight of other states, free energy calculations enable determination of the stability of a state, of kinetic barriers between states, and the relative weights of multiple competing states in equilibrium when the free energy differences are small. This is important when applying simulations to particular systems, and also crucial when parameterizing force fields, which need to give accurate results for a wide range of different systems.

A large number of different free energy calculation techniques have been developed. These include umbrella sampling(1, 2), steered molecular dynamics(3-5), and density of states based techniques(6-9). Each of these methods have advantages and drawbacks. Umbrella sampling requires previous knowledge of the free energy surface in order to pick parameters for each of the many simulation windows that will produce an efficient simulation, and may require multiple attempts with different parameters if the first choice leaves gaps of poor sampling. Steered molecular dynamics requires many independent trajectories, and often requires very slow simulations for accurate results. There are many density of states based techniques, but a common limitation is that they apply only to Monte Carlo simulations, which are unsuitable for atomistic simulations of large molecules, where molecular dynamics are much more feasible.

Metadynamics(10-12) is an attractive method for free energy calculation because its ability to calculate free energies even in the presence of very large barriers of unknown location and size, and its often fast rate of convergence. A limitation to metadynamics calculations has been the inability to simulate systems using multiple collective variables due to boundary artifacts. These artifacts arise when a collective variable is limited in its range in a way that is not periodic. An effective solution to this problem already exists when the collective variable space is one dimensional, however it does not generalize to higher dimensions.

In chapter 2 of this thesis, we will present a modification to the metadynamics algorithm that converges to the correct solution in any number of dimensions, regardless of the presence of boundaries. This expands the range of problems metadynamics can be applied to.

The remaining chapters will apply simulation methods to particular systems. In chapter 3, we will look at a class of synthetic protein-like molecules known as β-peptides. β-peptides are a class of synthetic protein like molecules. They differ from natural α-peptides in that they are composed of β-amino acids as monomers, which have one additional backbone carbon atom compared to naturally occurring α-amino acids. Like proteins, β-peptides with different sequences have different properties. We will use free energy calculations to examine the propensity of two peptides to arrange themselves in a particular orientation, and examine how this relates to self-assembly behavior.

In chapter 4, we will examine the effect of the sugar trehalose on the interaction of human islet amyloid polypeptide (hIAPP) with membranes. hIAPP is a peptide cosecreted with insulin from pancreatic β-cells, whose aggregation into fibrils in these cells is linked to diabetes. The rate of fibril formation is greatly increased by the presence of anionic membranes, however the mechanism of fibril formation is poorly understood. Trehalose is a disaccharide that has been demonstrated to inhibit the aggregation of several peptides. Knowing about inhibitors of hIAPP aggregation may help in designing therapies for diabetes. Using both simulations and experiments, we will examine the effect of trehalose on the aggregation of hIAPP. We find that in the case of hIAPP, trehalose actually promotes aggregation. Analysis of this data offers evidence about the mechanism of hIAPP aggregation.

1.1 References

1. Torrie, G. M., and J. P. Valleau. 1977. NON-PHYSICAL SAMPLING DISTRIBUTIONS IN MONTE-CARLO FREE-ENERGY ESTIMATION - UMBRELLA SAMPLING. Journal of Computational Physics 23:187-199.
2. Kumar, S., D. Bouzida, R. H. Swendsen, P. A. Kollman, and J. M. Rosenberg. 1992. THE WEIGHTED HISTOGRAM ANALYSIS METHOD FOR FREE-ENERGY CALCULATIONS ON BIOMOLECULES .1. THE METHOD. Journal of Computational Chemistry 13:1011-1021.
3. Isralewitz, B., J. Baudry, J. Gullingsrud, D. Kosztin, and K. Schulten. 2001. Steered molecular dynamics investigations of protein function. Journal of Molecular Graphics & Modelling 19:13-25.

4. Kosztin, I., B. Barz, and L. Janosi. 2006. Calculating potentials of mean force and diffusion coefficients from nonequilibrium processes without Jarzynski's equality. Journal of Chemical Physics 124.
5. Forney, M. W., L. Janosi, and I. Kosztin. 2008. Calculating free-energy profiles in biomolecular systems from fast nonequilibrium processes. Physical Review E 78.
6. Janosi, L., and M. Doxastakis. 2009. Accelerating flat-histogram methods for potential of mean force calculations. Journal of Chemical Physics 131.
7. Wang, F. G., and D. P. Landau. 2001. Efficient, multiple-range random walk algorithm to calculate the density of states. Physical Review Letters 86:2050-2053.
8. Engkvist, O., and G. Karlstrom. 1996. A method to calculate the probability distribution for systems with large energy barriers. Chemical Physics 213:63-76.
9. Kim, E. B., R. Faller, Q. Yan, N. L. Abbott, and J. J. de Pablo. 2002. Potential of mean force between a spherical particle suspended in a nematic liquid crystal and a substrate. Journal of Chemical Physics 117:7781-7787.
10. Bussi, G., A. Laio, and M. Parrinello. 2006. Equilibrium free energies from nonequilibrium metadynamics. Physical Review Letters 96:4.
11. Laio, A., and M. Parrinello. 2002. Escaping free-energy minima. Proceedings of the National Academy of Sciences of the United States of America 99:12562-12566.
12. Laio, A., and F. L. Gervasio. 2008. Metadynamics: a method to simulate rare events and reconstruct the free energy in biophysics, chemistry and material science. Reports on Progress in Physics 71:22.

Chapter 2: A Boundary Correction Algorithm for Metadynamics in Multiple Dimensions

2.1 Introduction

A major obstacle to the simulation of complex systems is the presence of large free energy barriers between local minima. Several methods have been proposed to overcome this problem. These include umbrella sampling[1,2], density of states based techniques[3,4] and, more recently, metadynamics [5-7]. Here we focus on the latter method, as it provides a powerful and yet simple tool for study of complex systems. In metadynamics, one or more collective variables are selected which are functions of the particle or atomic coordinates. The Hamiltonian of the system is altered by adding a biasing "hill" potential of the form

$$We^{-\sum_i \frac{(x_i - s_i)^2}{2\sigma_i^2}} \quad (\mathbf{1})$$

to distinct configurational states as they are visited. In Equation (1), s_i is any value of collective variable i, and x_i is the instantaneous value of the collective variable at time t. At any given time, the bias potential is given by the sum of the biases from all of the previously added hills. At long times, sampling of the collective variables is nearly uniform, and the negative of the bias potential provides an estimator of the free energy of the system as a function of the collective variables. Several variations on this method have been proposed, including well-tempered metadynamics and flux-tempered metadynamics, to name a few [8,9]. Here we focus on the original metadynamics approach, but the conclusions put forth in what follows hold for other variants as well, with only slight modifications to the argument.

A problem arises in metadynamics simulations in the vicinity of a boundary. As an example, an order parameter that is bounded between zero and unity is limited by a boundary at zero and a boundary at one. For a state point located near the middle of the collective variable space, hills on all sides of the point contribute to the free energy. In contrast, a boundary point exhibits a lack of hills on one or more sides, thereby leading to reduced biasing of that region.

In past work, the problems associated with boundaries have been addressed in several ways. For simulations where the free energy in the boundary region is not needed, an interval can be defined near the boundary where the force resulting from the bias potential is set to zero[10]. That is, some number, $s_{i,w}$, is chosen and, for a lower boundary at $s_i=0$, the biasing force is set to zero when $x_i<s_{i,w}$. This prevents the accumulation of large forces as the derivative of the bias potential near the boundary grows larger when the simulation progresses, but it precludes calculation of the free energy near the boundary.

Another approach is to use an “inversion condition” at the boundary [11]. In this algorithm, two parameters χ_1 and χ_2 are chosen. Assuming again a lower boundary at $s_i=0$, then for $s_i< \chi_1$, at every step when a hill is deposited, an additional hill with the same height and width is deposited centered at $-s_i$. If $s_i> \chi_1$, an additional hill is also added centered at $-s_i$; however, the height is adjusted to enforce a linear profile near the boundary. For a linear profile at the boundary, the following condition would be satisfied:

$$V(-s_i, t) - 2V(0, t) + V(s_i, t) = 0 \quad (\mathbf{2})$$

In order to coerce the profile to approach linearity, the height of the added Gaussian is multiplied by a factor w, given by

$$w = \frac{[2V(0,t) - V(-s_i,t) - V(s_i,t)]}{1 + \left(\frac{s_i}{\chi_1 \chi_2}\right)^{10}} \quad (\mathbf{3})$$

This factor may be positive or negative, as needed, to reduce deviations from linearity. The denominator is approximately unity for $s_i < \chi_1\ \chi_2$, and rapidly approaches 0 for $s_i > \chi_1\ \chi_2$. A maximum height cutoff is also usually employed to improve stability, so that in cases where the above formula exceeds the cutoff (in absolute value), the cutoff value (or the negative of it) is used instead[12]. This method leads to a linear profile near the boundary in the case of a one-dimensional simulation, but suffers from two drawbacks. First, the method still leads to systematic errors at points near the joint boundaries of multiple collective variables. This means, for example, that in a simulation with two collective variables, there will still be artifacts at the four corners of the corresponding two-dimensional free energy surface. The other drawback is that, at long times, sampling of the collective variable space is not uniform, but instead one can often observe 'ringing' at the boundary, where the histogram shows a large maximum and a large minimum very close to the boundary. This is not desired because it leads to systematic under-sampling of certain states.

Here we propose a method that overcomes these limitations. The method is derived by finding an exact expression for the errors that accumulate due to boundary effects at every step. This leads to a condition that must be satisfied by modifications to the Gaussian form of the bias potential in a manner that avoids boundary artifacts. Two modifications satisfying these conditions are proposed, and their validity is illustrated in the context of two different examples.

2.2 Methods

A necessary condition for convergence of metadynamics simulations is that the bias potential change over time, on average, only by the addition of a constant. By this we mean that, given a large number of independent metadynamics simulations that have all reached convergence, where the bias potential corresponds to the negative of the free energy, the average effect of continuing each simulation until one more hill has been deposited must be that the average bias remains the negative of the free energy.

However, in traditional metadynamics simulations with no boundary correction, the average energy added by a hill is not constant. Let us assume that the metadynamics simulation is performed in N variables, $(x_1,x_2,\ldots x_N)=\vec{x}$, and that these collective variables have lower bounds $(L_1,L_2,\ldots L_N)=\vec{L}$ and upper bounds $(U_1,U_2,\ldots U_N)=\vec{U}$. Then the average change in the bias potential at point $\vec{x}=\vec{s}$ resulting from the addition of one hill is:

$$\overline{\Delta V}(\vec{s}) = \iint \ldots \int_{\vec{L}}^{\vec{U}} We^{-\sum_i \frac{(x_i-s_i)^2}{2\sigma_i^2}} P(\vec{x})d\vec{x} \quad \mathbf{(4)}$$

where $P(\vec{x})$ is the probability of visiting state $\vec{x}$. For a converged simulation, the bias potential is equal to the negative of the free energy, and $P(\vec{x})$ is a uniform distribution:

$$\mathrm{P}(\vec{x}) = \prod_{i=1}^{N} \frac{1}{(U_i - L_i)} \quad \textbf{(5)}$$

Under the assumption of a uniform probability distribution, the average change to the bias potential can be calculated by evaluating the integral in Equation (4), resulting in the following expression for $\overline{\Delta V}(\vec{s})$:

$$\overline{\Delta V}(\vec{s}) = W \prod_{i=1}^{N} \sqrt{\frac{\pi}{2}} \frac{\sigma_i}{(U_i - L_i)} [\mathrm{erf}\left(\frac{s_i - L_i}{\sqrt{2}\sigma_i}\right) + \mathrm{erf}\left(\frac{U_i - s_i}{\sqrt{2}\sigma_i}\right)] \quad \textbf{(6)}$$

Expression (6) is not constant, and so the simulation is not converged when $\mathrm{P}(\vec{x})$ is uniform. This equation provides the basis for all of the correction schemes we consider below.

In what follows, the unmodified Gaussian hill will be denoted by $V_G(\vec{x}, \vec{s})$:

$$V_G(\vec{x}, \vec{s}) = \ W e^{-\sum_i \frac{(x_i - s_i)^2}{2\sigma_i{}^2}} \quad \textbf{(7)}$$

To find a valid boundary correction scheme, we must find functions $\mathrm{V}_\mathrm{M}(\vec{x}, \vec{s})$ that satisfy

$$\iint \dots \int_{\vec{L}}^{\vec{U}} \mathrm{V}_M(\vec{x}, \vec{s}) \mathrm{P}(\vec{\mathrm{x}}) d\vec{x} = C \quad \textbf{(8)}$$

Assuming we do this in a manner that keeps $\mathrm{P}(\vec{x})$ uniform, this condition can be expressed as

$$\iint \dots \int_{\vec{L}}^{\vec{U}} \mathrm{V}_M(\vec{x}, \vec{s}) \prod_{i=1}^{N} \frac{1}{(U_i - L_i)} d\vec{x} = C \quad \textbf{(9)}$$

One way to satisfy Equation (9) is to multiply V_G by a factor that makes the integral constant; since the probability integral is over $\vec{x}$, as opposed to $\vec{s}$, it can be seen that the simplest way to meet that condition is to define

$$V_M(\vec{s}) = \frac{We^{-\sum_i \frac{(x_i - s_i)^2}{2\sigma_i^2}}}{\prod_{i=1}^{N} \sqrt{\frac{\pi}{2}} \frac{\sigma_i}{(U_i - L_i)} [\operatorname{erf}\left(\frac{s_i - L_i}{\sqrt{2}\sigma_i}\right) + \operatorname{erf}\left(\frac{U_i - s_i}{\sqrt{2}\sigma_i}\right)]} = \frac{V_G}{\overline{\Delta V_G}} \quad \mathbf{(10)}$$

where $\overline{\Delta V_G}$ denotes the average bias added with uncorrected Gaussians, as given by Equation (6). Equation (10) provides an exact correction to boundary errors in any number of dimensions.

Other forms for the correction are also possible. We could, for example, use an additive expression. To do so, we simply assume $V_M = V_G + V_B$, subject to

$$\iint \dots \int_{\vec{L}}^{\vec{U}} V_B \prod_{i=1}^{N} \frac{1}{(U_i - L_i)} d\vec{x}$$

$$= -W \prod_{i=1}^{N} \sqrt{\frac{\pi}{2}} \frac{\sigma_i}{(U_i - L_i)} \left[\operatorname{erf}\left(\frac{s_i - L_i}{\sqrt{2}\sigma_i}\right) + \operatorname{erf}\left(\frac{U_i - s_i}{\sqrt{2}\sigma_i}\right)\right] + C \quad \mathbf{(11)}$$

where *C* is an arbitrary constant that can be set *C*=0. The simplest additive correction is therefore

$$V_B = -W \left(\frac{\pi}{2}\right)^{\frac{N}{2}} \prod_{i=1}^{N} \left[\operatorname{erf}\left(\frac{s_i - L_i}{\sqrt{2}\sigma_i}\right) + \operatorname{erf}\left(\frac{U_i - s_i}{\sqrt{2}\sigma_i}\right)\right] \quad \mathbf{(12)}$$

The additive correction of Equation (12) has the advantage of being faster to compute than either the multiplicative correction or the invert condition. This is because the positional dependence of the boundary term remains constant, up to a multiplicative constant. The total boundary correction at any point in time is simply V_B times the number of hills deposited up to that time.

The disadvantage of the additive correction, however, is that it represents a global correction that only properly compensates for boundary effects in the long-time limit, once the simulation has converged. The multiplicative correction is a local correction that tends to converge more rapidly, at the expense of requiring more demanding calculations.

Note that these two methods are not the only ones that satisfy Equation (8). There are many other corrections, both additive and multiplicative, as well as other functional forms. Among additive corrections, any potential of the form

$$\mathrm{V}_B = -Wf(\vec{x},\vec{s})\left(\frac{\pi}{2}\right)^{\frac{N}{2}}\prod_{i=1}^{N}\left[\operatorname{erf}\left(\frac{s_i - L_i}{\sqrt{2}\sigma_i}\right) + \operatorname{erf}\left(\frac{U_i - s_i}{\sqrt{2}\sigma_i}\right)\right] \quad (\mathbf{10})$$

subject to

$$\iint \dots \int_{\vec{L}}^{\vec{U}} f(\vec{x},\vec{s})d\vec{x} = 1 \quad (\mathbf{11})$$

will work. In all of this, we have assumed that we are only using functions of the coordinates of the system at a given time and of the collective variables directly. More general functions are possible, such as functions of the bias potential itself. The invert condition is of this last type, but, in general, it does not satisfy Equation 8. The two that we present here are merely methods that in our experience offer advantages over available alternatives from the current literature.

2.3 Model Systems

We test these methods on two model systems. All simulations were carried out in gromacs 4.5.5[13], using the PLUMED plugin[14], which was modified to implement this algorithm. The modified version of the code is available on the authors' website. The first system consists of two non-interacting circular particles evolved under Brownian dynamics and restricted to two dimensions. The collective variables used here are the distance between the particles along the x-axis and the distance between the particles along the y-axis. The free energy profile of such a system should be flat. The friction coefficient was 6 amu/ps. The temperature was set to 300K. Simulations were performed with a time step of 1fs. Hills were deposited every 500 time steps, with a height of 0.02 kJ/mol. σ was set to 0.4nm. The box was a cube with side 4nm. The particles were started at a distance of 1nm in x, and 0nm in y and z.

This system was simulated using four variants: Using no boundary correction, the standard invert condition described by Equations (2) and (3), and using both the additive and multiplicative methods described here. For the invert condition, parameters were set to the PLUMED defaults, $\chi_1=1.6\sigma$ and $\chi_2=6\sigma$, with the maximum height cutoff for w being 4.

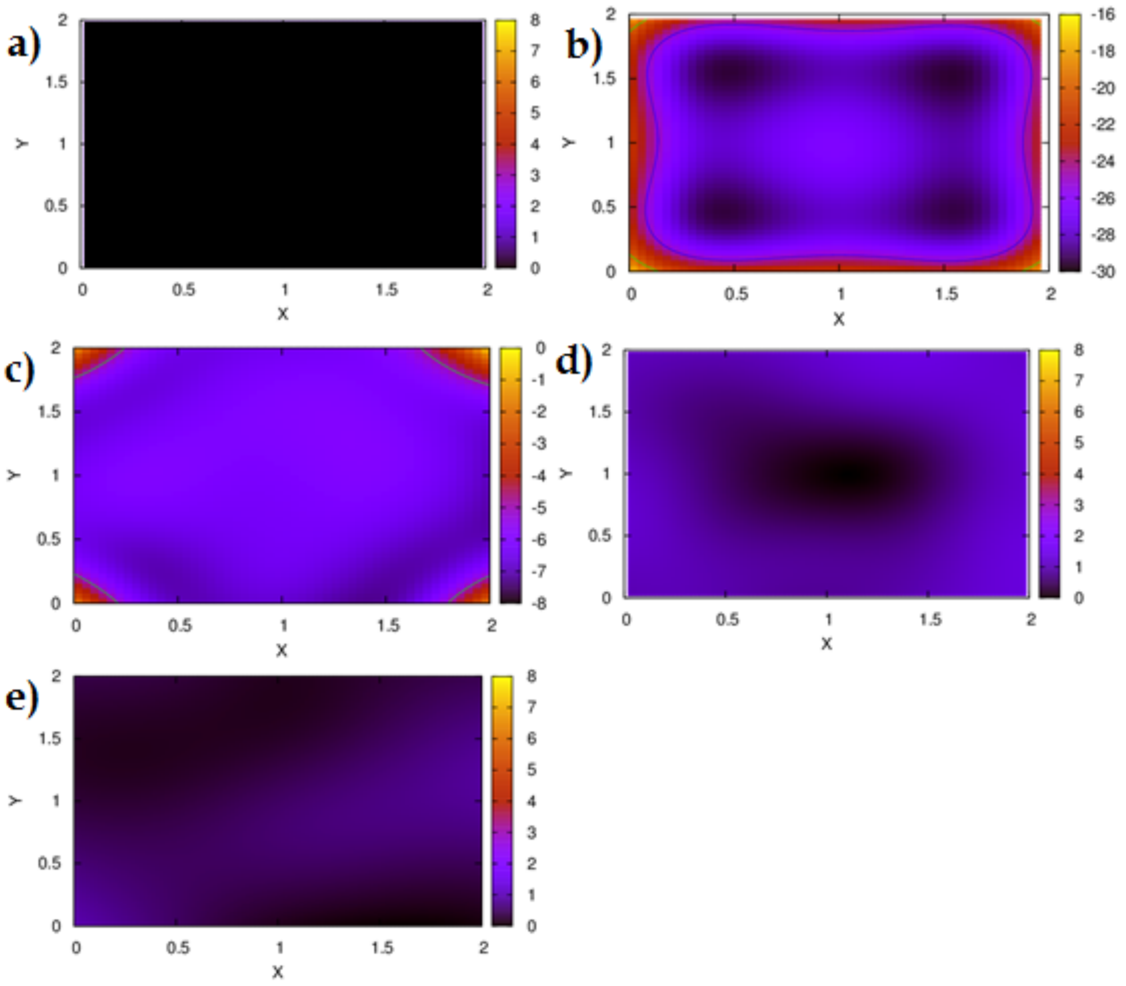

Figure 2-1: Free energy for non-interacting model system. Exact free energy (a) using no boundary correction (b), (different scale from other figures), inversion condition (c), additive algorithm (d), and multiplicative methods from this paper (e). All energy units are kJ/mol.

Results for the three cases are shown in Figure 1. Since the free energy in this case is known to be flat, any deviation from uniformity represents an error. From the figure, it is clear that the invert condition fails at points where two boundaries meet; in contrast, the algorithms presented here lead to a uniform free energy surface.

Second, we simulated an alanine dipeptide in vacuum using Langevin dynamics. The temperature was set to 300K, and the friction factor was $5ps^{-1}$. The CHARMM27 force field was used. We used the cosines of the ϕ and ψ dihedral angles as collective variables; this cosines were used in order to introduce a boundary into the collective variables and demonstrate the validity of the proposed approach. The system was simulated for 4 ns using the invert condition method and with the multiplicative correction. To calculate the free energy precisely, the bias from the error function was added to a long (125ns) molecular dynamics simulation, and the histogram from this simulation was used to correct the free energy surface. Since molecular dynamics is free from any boundary artifacts, its output should correspond to the correct free energy surface.

The results are shown in Figure 2. The corrected free energy surface shows two minima, one centered around cos(φ)=0, cos(ψ)=0.25, and one in the cos(φ)=-1, cos(ψ)=-1 corner. Since the inversion method tends to create artificial free energy maxima at the corners of the free energy surface, it can be seen that the minimum in the corner becomes highly distorted, and shifts to around cos(φ)=-0.7. The method presented here does not exhibit such distortions.

In order to examine the computational performance of the proposed methods, in Figure 3 we show how the error in this corner changes over time. It is calculated by generating the free energy surface up to a given time, averaging over half the previous simulation time. This free energy surface is subtracted from the MD corrected free energy surface. The arbitrary free energy constant is removed by subtracting the average difference, and the absolute value of the difference is averaged over the corner region. The invert condition method does not converge, and the error grows after quickly reaching a minimum value. The multiplicative correction error decreases steadily over time. Because additional hills need to be added near the boundary to enforce the invert condition, while no additional hills are needed with the multiplicative correction, the multiplicative correction also uses less CPU time.

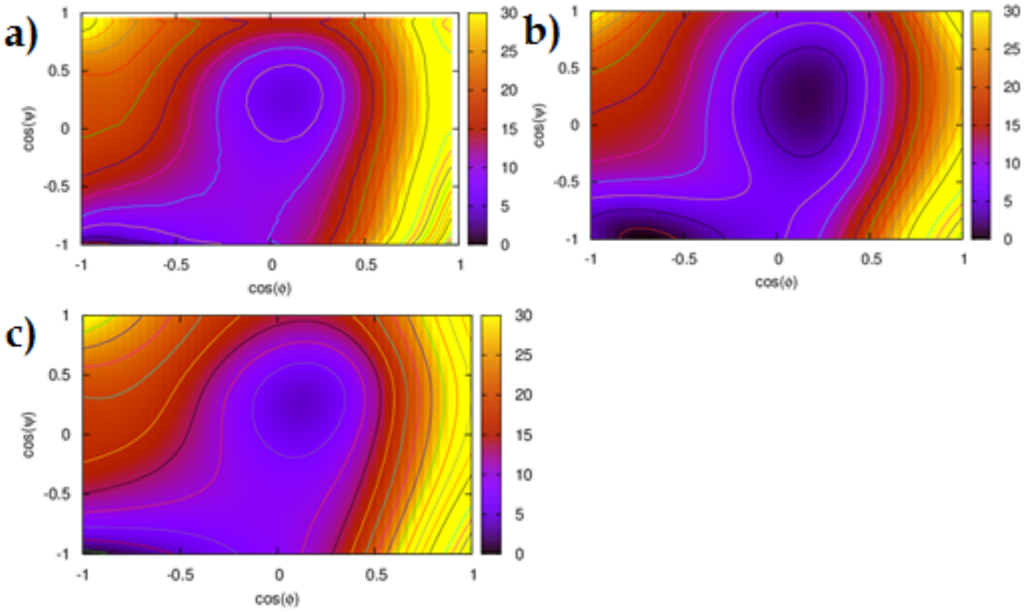

Figure 2-2: Free energy profile for alanine dipeptide model system is, from a simulation with boundary errors corrected over a 125ns molecular dynamics calculation using the bias from the multiplicative algorithm presented here(a). The free energy of the same system using traditional metadynamics with a standard invert condition is shown in (b), while the free energy generated using the multiplicative algorithm presented here is shown in (c). All energy units are kJ/mol.

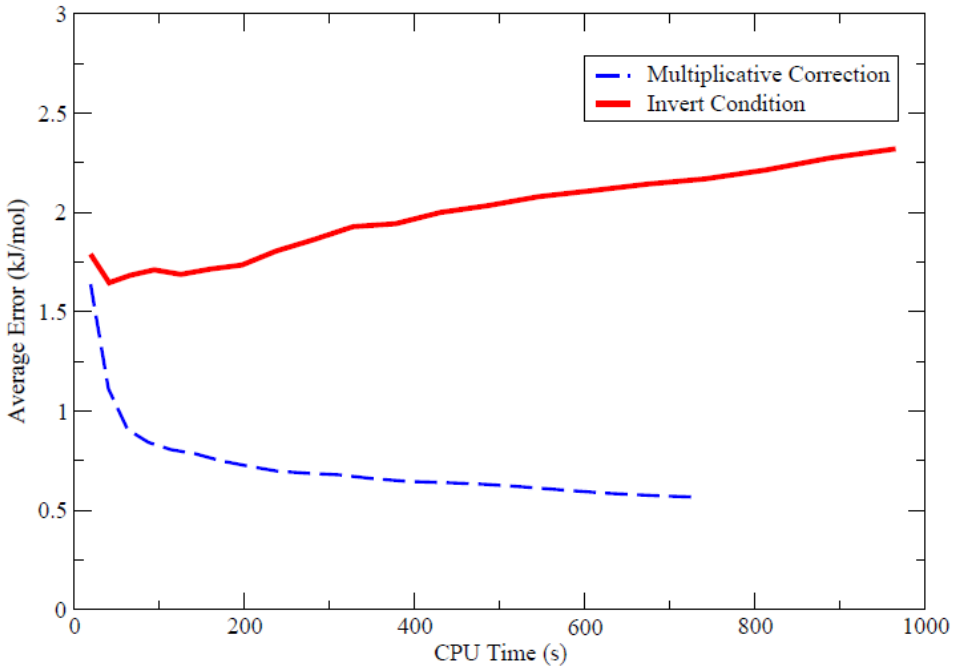

Figure 2-3: Average absolute error as a function of CPU time for the invert condition and multiplicative correction in the free energy minimum corner (defined as cos(φ)<-0.75, cos(ψ)<-0.75). Both systems were simulated for 4ns of simulation time, with the multiplicative method system taking 650s of CPU time, and the invert condition system taking 1000s of CPU time.

2.4 Conclusion

Metadynamics simulations provide an efficient means for calculation of the free energy of relatively complex molecular systems. One of the advantages of metadynamics over other simulation techniques is that it is able to generate free energy surfaces in multiple dimensions in an efficient manner. When some of these dimensions are bounded, however, one needs to include an invert condition designed to correct for boundary effects. In the past, such a correction has only been presented for unidimensional systems, thereby limiting severely the general applicability of metadynamics. In this work, we have presented an alternative means for eliminating boundary errors. In one dimension, the method proposed here is superior to the traditional invert condition. More importantly, the proposed method is applicable in any number of dimensions. The applicability of the method was demonstrated with two numerical examples, leading to satisfactory results in both cases. This method has now been implemented in public domain codes, and is available for general use by the authors. We expect the proposed the method to find widespread use in simulations of complex fluids and materials.

2.5 References

[1] G.M. Torrie, J.P. Valleau, Journal of Computational Physics 23 (1977) 187.

[2] S. Kumar, D. Bouzida, R.H. Swendsen, P.A. Kollman, J.M. Rosenberg, Journal of Computational Chemistry 13 (1992) 1011.

[3] O. Engkvist, G. Karlstrom, Chemical Physics 213 (1996) 63.

[4] F.G. Wang, D.P. Landau, Physical Review Letters 86 (2001) 2050.

[5] G. Bussi, A. Laio, M. Parrinello, Physical Review Letters 96 (2006) 4.

[6] A. Laio, M. Parrinello, Proceedings of the National Academy of Sciences of the United States of America 99 (2002) 12562.

[7] A. Laio, F.L. Gervasio, Reports on Progress in Physics 71 (2008) 22.

[8] A. Barducci, G. Bussi, M. Parrinello, Physical Review Letters 100 (2008) 4.

[9] S. Singh, C.C. Chiu, J.J. de Pablo, Journal of Statistical Physics 145 (2011) 932.

[10] B. F., C. P., P. F., L. A., Protein folding and ligand-enzyme binding from bias-exchange metadynamics simulations Current Physical Chemistry, (In Press).

[11] Y. Crespo, F. Marinelli, F. Pietrucci, A. Laio, Physical Review E 81 (2010) 4.

[12] V. Babin, C. Roland, C. Sagui, Journal of Chemical Physics 128 (2008) 7.

[13] B. Hess, C. Kutzner, D. van der Spoel, E. Lindahl, Journal of Chemical Theory and Computation 4 (2008) 435.

[14] M. Bonomi, D. Branduardi, G. Bussi, C. Camilloni, D. Provasi, P. Raiteri, D. Donadio, F. Marinelli, F. Pietrucci, R.A. Broglia, M. Parrinello, Computer Physics Communications 180 (2009) 1961.

Chapter 3: Dimerization of Helical Beta-Peptides in Solution

3.1 Introduction

Oligomers of β-amino acids, known as β-peptides, are a class of synthetic protein-like molecules that have received considerable attention as a result of their ability to form well defined secondary structures. Compared to the α-amino acids found in proteins, β-amino acids have one additional backbone carbon atom. That additional backbone carbon atom increases the palette of available residues, and offers the possibility of introducing ring containing structures into the peptide backbone. Certain β-peptides form highly stable and predictable helical secondary structures (1-7). In particular, introducing five membered cyclic residues into the β-peptide stabilizes a helical secondary structure known as the 14-helix, in which each hydrogen bonded ring has fourteen members. In this type of helix, each β-amino acid forms a hydrogen bond with the β-amino acids located three residues away. Figure 1 illustrates a typical β-peptide helix for a ten-residue long β-peptide, and shows typical dimensions for the helix. These helices are highly stable, and form with a lower minimum number of residues than the helices of natural peptides (8).

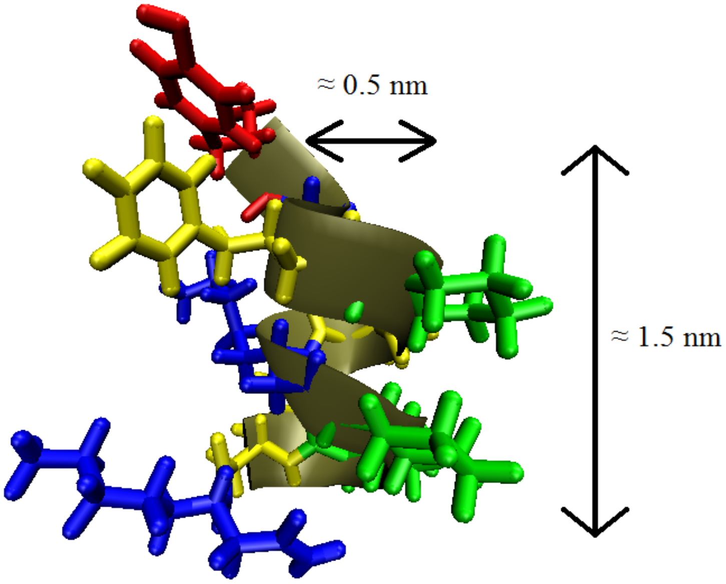

Figure 3-1: A 14-helical β-peptide. The residues are colored as follows: Red - β^3-hTyr ; Green – ACHC; Blue - β^3-hLys ; Yellow - β^3-hPhe

Beyond their ability to form stable secondary structures, β-peptides also exhibit a rich self-assembly behavior. In this regard, β-peptides are particularly attractive in that one can control their secondary structure and ensure that it is preserved throughout the aggregation process. Furthermore, one can also control the three-dimensional presentation of the molecules' various functional groups and examine the role of structure on intermolecular interactions. This feature is illustrated in Figure 2, which provides a schematic representation of the four β-peptides considered in this work. The four peptides have two sets of residues, and there are two isomers of each. In one isomer, referred to as the globally amphiphilic (GA) isomer, each side of the helix contains either only hydrophobic or only hydrophilic groups. In the non-globally amphiphilic (NGA) isomer, each face of the helix contains both types of residue. The ability to present distinct chemical moieties on a particular "face" of the molecule is of interest in fundamental studies of peptide association in solution because it allows one to extract unambiguous conclusions about the role of sequence on association. A notable example is provided by recent work in which distinct sequences of short β-peptides induced the formation of liquid crystalline phases (9). More generally, different types of aggregates have been observed depending on sequence. Some β-peptides form globular aggregates, while others form fibers (10). One fiber aggregate formed by a β-peptide sequence was characterized as consisting of hollow cylinders (11).

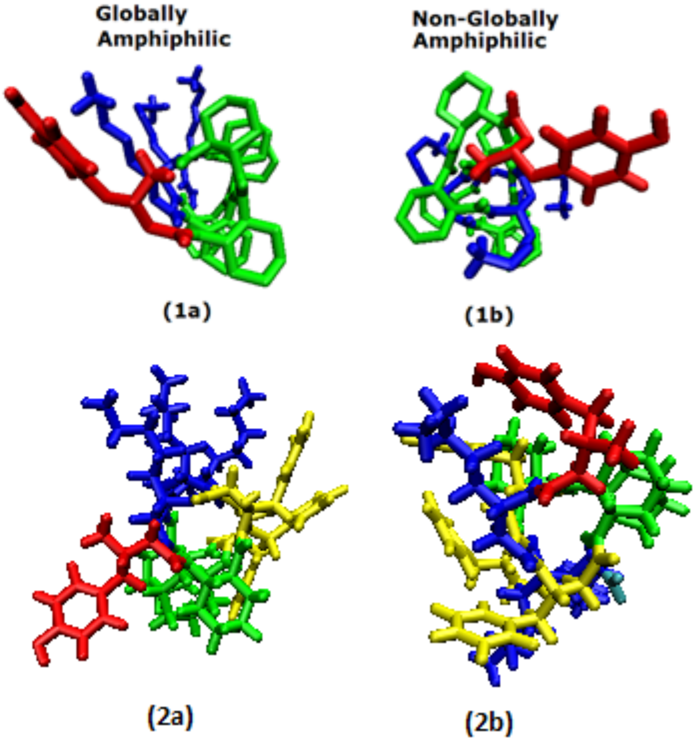

Figure 3-2: Illustration of the four peptides studied showing globally amphiphilic and non-globally amphiphilic display of hydrophobic and hydrophilic groups

Recent experiments have revealed a broad range of self assembling behaviors of the four peptide sequences considered here, shown in Figure 3. The β-amino acids contained in these β-peptide sequences are analogues of the α-amino acids tyrosine (β^3-hTyr), lysine (β^3-hLys), phenylalanine (β^3-hPhe), as well as a β-amino acid with a five membered ring, trans-2-aminocyclohexanecarboxylic acid (ACHC). The four peptides consist of two globally amphiphilic β-peptides, and non-globally amphiphilic isomers of each of these. Experimentally, the peptide with sequence labeled 1a in Figure 3 exhibits a liquid crystal phase, while its non-globally amphiphilic isomer (1b) does not. However, in the case of β-peptide 2, the pattern is reversed: the globally amphiphilic isomer (2a) does not form a liquid crystal phase, but the non-globally amphiphilic does.

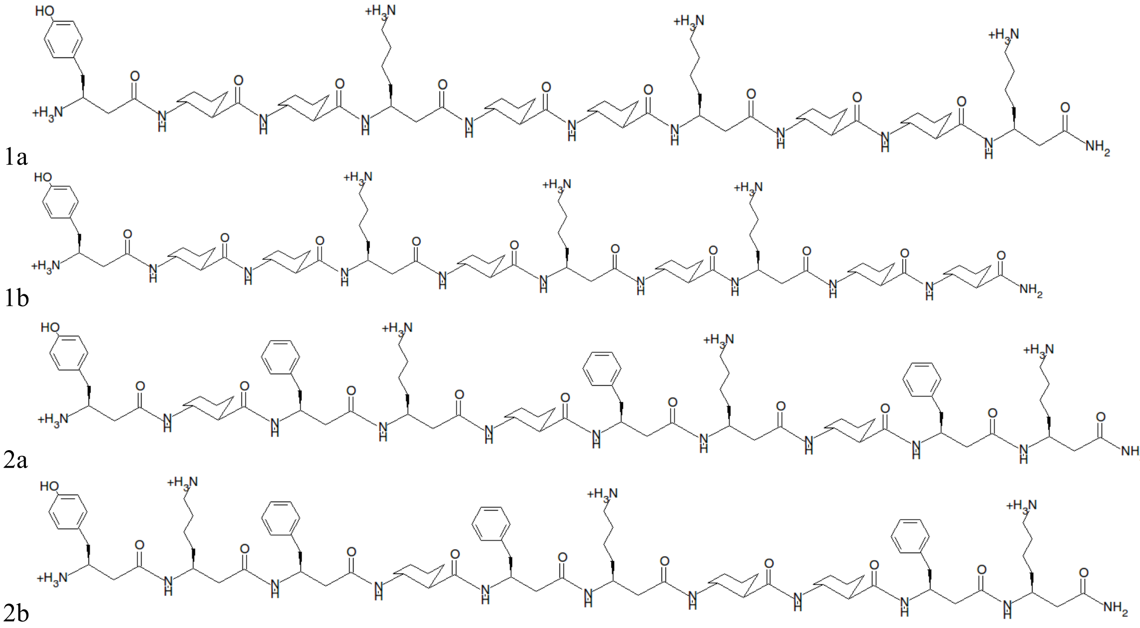

Figure 3-3: Structures of the four β-peptides

According to Onsager Theory, a liquid crystal phase can be formed by large anisotropic molecules due to excluded volume effects (12). Small molecules can also form a liquid crystal phase in a similar manner if they self-assemble into larger, highly anisotropic aggregates. This self-assembly process has been extensively studied for the case of globally amphiphilic molecules. In such molecules, the hydrophobic faces tend to aggregate, leading to anisotropic structures such as lamellae or rod shaped micelles (13). The causes of a liquid crystal phase formed from non-globally amphiphilic small molecules are less well understood.

The aim of this paper is to gain an understanding of how β-peptide sequence influences aggregation and ultimately the formation of the liquid crystal phase by examining the free energy of interaction between two molecules in solution. We do so by resorting to molecular simulations of atomistic models of these four peptides. The resulting "potential of mean force" can be used to interpret aggregation experiments, and it can also serve as a guide to formulate coarse grain models for study of aggregation in solution. Previous computational studies of β-peptide aggregation have involved calculation of the potential of mean force as a function of distance between two peptides. Miller et al. calculated the potential of mean force for the four peptides mentioned above using constraint-force simulations of atomistic representations of the molecules (14). Subsequent simulations of the same molecules by Mondal et al. found global minima for all the peptides using umbrella sampling (15). While the models adopted in these studies were slightly different, the results of these two studies are not fully consistent with each other. Furthermore, Mondal et al. found that the different force field parameters in use for β-peptides gave similar aggregation behavior in their umbrella sampling simulations.

Pomerantz et. al. (10)observed the phase behavior of the four peptides studied here and proposed that highly anisotropic aggregates are responsible for the liquid crystal forming behavior of the two peptides that formed this phase, although they did not propose a molecular level explanation for the different aggregation behavior of the peptides. Since a high degree of anisotropy is required in the proposed aggregates, it is therefore important to understand how the faces of these β-peptides approach each other to gain a molecular level understanding of the aggregation behavior. As mentioned above, past computational studies relied only on uni-dimensional calculations of the potential of mean force along the separation between the centers of mass of two molecules. In order to investigate the role of relative orientation on the interaction between two molecules and identify the source of discrepancies between previous calculations, in this work we introduce a second variable along which to sample interactions and we generate free energy surfaces as a function of both distance and orientation. More specifically, we define a helix angle variable with a vector across the helix on each peptide, and control the angle between these two vectors. This is illustrated in Figure 4; a precise definition is given in the Methods section. Recently proposed metadynamics simulations are used to facilitate sampling of configurational space (16). Our results indicate that the peptides which show both a strong tendency to aggregate and a strong conformational preference for certain helix angles form liquid crystal phases, while the others do not. Our results also show that past simulations might have been hampered by the existence of deep local minima within the corresponding two dimensional free energy surfaces, thereby explaining the inconsistencies between different literature reports

3.2 Materials and Methods

Summary of β-peptides studied		
1a	(β^3-hTyr)-[ACHC-ACHC-(β^3-hLys)]$_3$	Forms liquid crystal phase, aggregates
1b	(β^3-hTyr)-[ACHC-ACHC-(β^3-hLys)]-[ACHC-(β^3-hLys)-ACHC]-[(β^3-hLys)-ACHC-ACHC]	Does not form liquid crystal phase, does not aggregate
2a	(β^3-hTyr)-[ACHC-(β^3-hPhe)-(β^3-hLys)]$_3$	Forms aggregates, but not liquid crystal
2b	(β^3-hTyr)-[(β^3-hLys)-(β^3-hPhe)-ACHC]-[(β^3-hPhe)-(β^3-hLys)-ACHC]-[ACHC-(β^3-hPhe)-(β^3-hLys)].	Forms liquid crystal with cylindrical structure

Table 1: Description of the four β-peptides studied. The first column gives the abbreviations used in this paper. The second column gives a β-amino acid sequence. The β-amino acids are abbreviated as follows: β^3-hTyr =β^3homotyrosine, ACHC = trans-2-aminocyclohexanecarboxylic acid, β^3-hLys = β^3homolysine, and β^3-hPhe = β^3homophenylalanine. Chemical structures for each of these amino acids are represented in the structure of peptide 2a in figure 1, which contains all of the β-amino acids mentioned.

The chemical structures of the peptides considered in this work are given in Figure 3. For completeness, their sequences are given in Table 1, along with key characteristics describing their tendency to aggregate. Most of our simulations were performed in cubic boxes of side length 5.4 nm, and included approximately 5300 water molecules. A 200ns simulation was also performed for peptide 1a with a larger box size, 6nm on each side and 7015 water molecules, to examine finite size effects. Initial structures for each peptide were generated by using 14-helical β-peptide structures for the four peptides taken from earlier simulations(4). The peptides were then replicated, so that two identical peptides were initially placed at an arbitrarily selected separation of 2nm. For that separation the interactions between the molecules are small. The system was then solvated with TIP3P water and counter-ions to preserve electroneutrality, and equilibrated during 4ns of molecular dynamics simulations at constant pressure and temperature. These structures were used as the initial configuration for NPT metadynamics simulations. Four replicas of each of the systems were created, for use in the bias exchange implementation discussed later. The CHARMm27 all atom force field was used (17), with parameters developed for β-peptides from reference (5). This force field was developed based on an approach that optimized parameters with respect to ab initio and experimental data, with parameters specifically designed to capture aromatic interactions in the case of aromatic amino acids (18). A particle-mesh Ewald sum was used for long-range electrostatic interactions with a short range cut-off of 10 Å and a maximum relative error of 10^{-5}(19). A cut-off of 10 Å was also used for Lennard-Jones interactions. Bonds were constrained with the LINCS algorithm, and a time step of 0.002 ps was used. The velocity rescaling thermostat was used for temperature coupling(20), with a temperature coupling parameter of 0.2 ps. The pressure was maintained at 1 bar using the Berendsen barostat with a time constant of 1ps and a compressibility of $4.5 \cdot 10^{-5}$ bar^{-1}.

All simulations were performed using the gromacs (21) simulation package. The PLUMED (22) metadynamics plugin was used to enhance sampling. Hills were deposited every 200 time steps with a height of 0.1 kJ/mol. A wall potential was employed on the reaction coordinate at 2.5 nm to avoid sampling a region with artifacts arising from the periodic boundary conditions. We adopted a bias exchange implementation in which four replicas of the system are simulated (23). Two order parameters were considered in these simulations: the distance between the α-carbon of the fifth residue of each peptide, and the helix angle between two molecules. As illustrated in Figure 4, the helix angle is provided by the angle between vectors defined on each peptide. The vector on each peptide points from the α-carbon of the fifth residue to the β-carbon of the sixth residue. The helix angle is the angle between the vectors of the two peptides. The four replicas of the system consisted of one in which the biasing potentials for both reaction coordinates are excluded, one in which only the distance coordinate potential is used, one in which only the angle coordinate potential is used, and one in which the potentials for both order parameters are used. Only this last box is actually analyzed for results. Periodically, a swap between the configurations in the boxes is proposed. The swap between boxes ‘a’ and ‘b’ is accepted with probability

$$p_{ab} = \min\left(1, \beta\left[V_{bias}^{a}(x^{a},t) + V_{bias}^{b}(x^{b},t) - V_{bias}^{a}(x^{b},t) - V_{bias}^{b}(x^{a},t)\right]\right) \qquad (1)$$

Swap moves were proposed every 200 steps, consistent with the range of swap frequencies that has been used successfully in past simulations of protein systems with these methods (23, 24). For each peptide, simulations were performed for 200ns. The free energy was calculated from the first 150 ns of data, and recalculated after an additional 50ns. The free energy minima did not change location or change magnitude by more than 3kJ/mol, indicating good convergence.

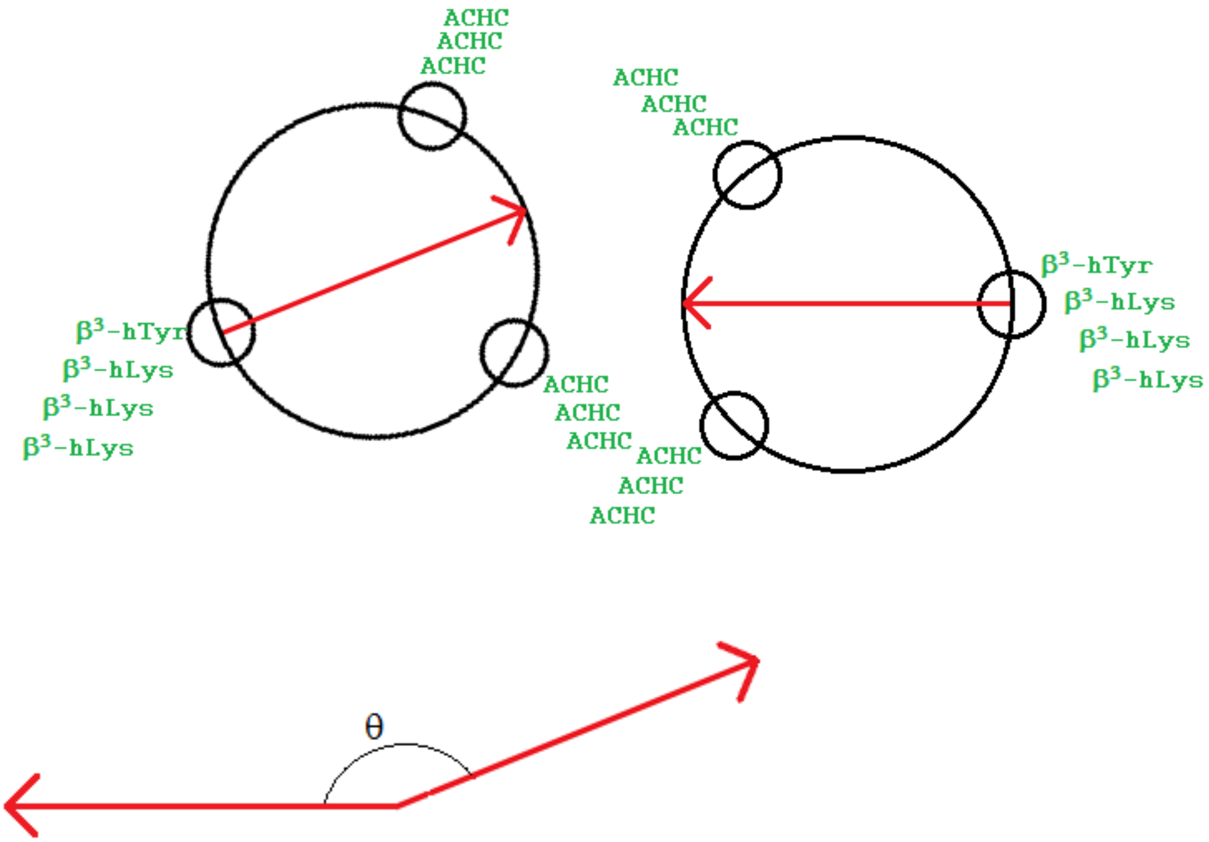

Figure 3-4: Illustration of the definition of the helix angle. In this figure peptide 1a is represented schematically. Here the two peptides align with their end-to-end vectors parallel. A vector is defined between two fixed atoms on the helix backbone for each peptide (the α-carbon of the fifth residue and the β-carbon of the sixth residue). In this case the angle is near 180°.Figure 5: Free energy surface for peptide 1a as a function of distance and helix angle in units of kJ/mol. Two deep free energy minima appear. They each correspond to the peptides aligning with hydrophobic faces pointing towards each other, with the end-to-end vectors nearly parallel in one case, and nearly anti-parallel in the other.

3.3 Results and Discussion

Figure 5 shows results from the two-dimensional bias exchange simulations for peptide 1a. Peptide 1a is the globally amphiphilic peptide with six cyclic ACHC groups that is experimentally found to form a liquid crystal phase. For peptide 1a, the free energy surface exhibits two distinct minima of approximately equal depth as a function of the helix angle, with angles close to 0 and 180° being preferred. The configuration at the minimum near 180° is similar to that represented in Figure 4, with a representative frame shown in Figure 7. The minimum near 0° is related, with the hydrophobic groups facing one another, but the peptides' end-to-end vectors align in an anti-parallel configuration, with the N-terminus of one peptide near the C-terminus of the other. Figure 5a shows results for peptide 1a performed on a larger box size, at the same conditions. A comparison between Figures 5 and 5a indicates that our simulations do not appear to suffer from finite size effects. The two free energy surfaces are very similar, with differences that are well within the statistical uncertainty of our results and had a root mean square difference of 0.4 kT.

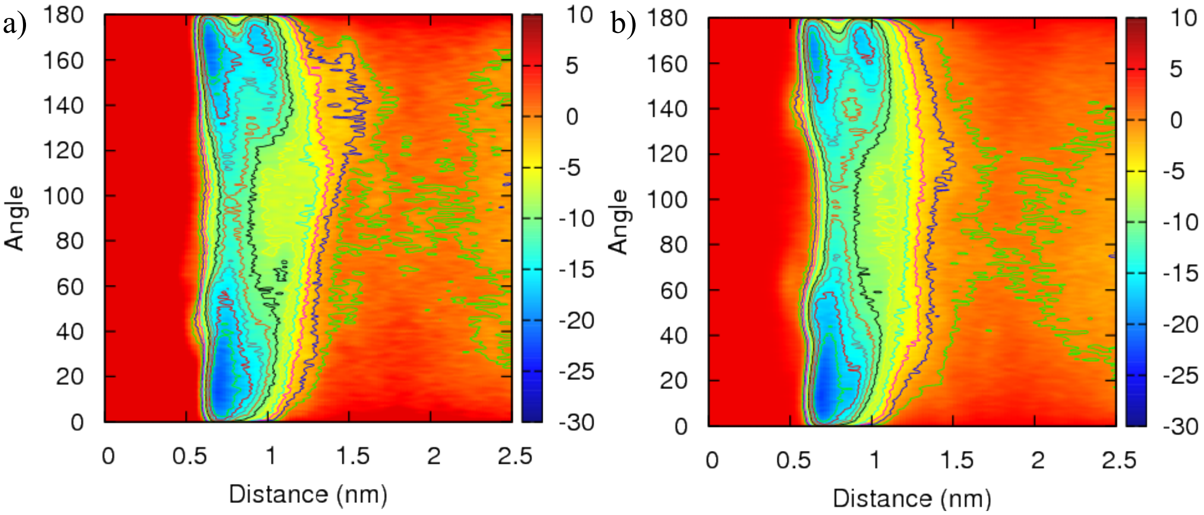

Figure 3-5: Free energy surface for peptide 1a as a function of distance and helix angle in units of kJ/mol for a cubic simulation box of 5.4nm(a) and 6nm(b). There are two deep free energy minima at a separation of around 0.7nm, one with a high helix angle corresponding to a parallel configuration of the end-to-end vectors and one with a low helix angle corresponding to anti-parallel end-to-end vectors. No finite size effects are apparent.

Figure 5b shows the free energy surface for peptide 1a after 200 ns of a bias exchange metadynamics simulations, but with the length of the cubic box changed from 5.4nm to 6nm. The free energy minima are in the same location, and the depths and widths of the minima are the same within the statistical uncertainty of our simulations. The differences in the free energy profiles are very small. We conclude from these results that finite size effects are unlikely to have a significant effects on the free energy profiles reported in this work.

Peptide 1b is the non-globally amphiphilic isomer of peptide 1a. Experimentally, it is not found to form a liquid crystal phase. The free energy surface for this peptide is shown in Figure 6. Peptide 1b exhibits only a weak minimum in free energy,5kJ/mol at its deepest, which is much less than the free energy minimum for peptide 1a as a function of either distance or angle.

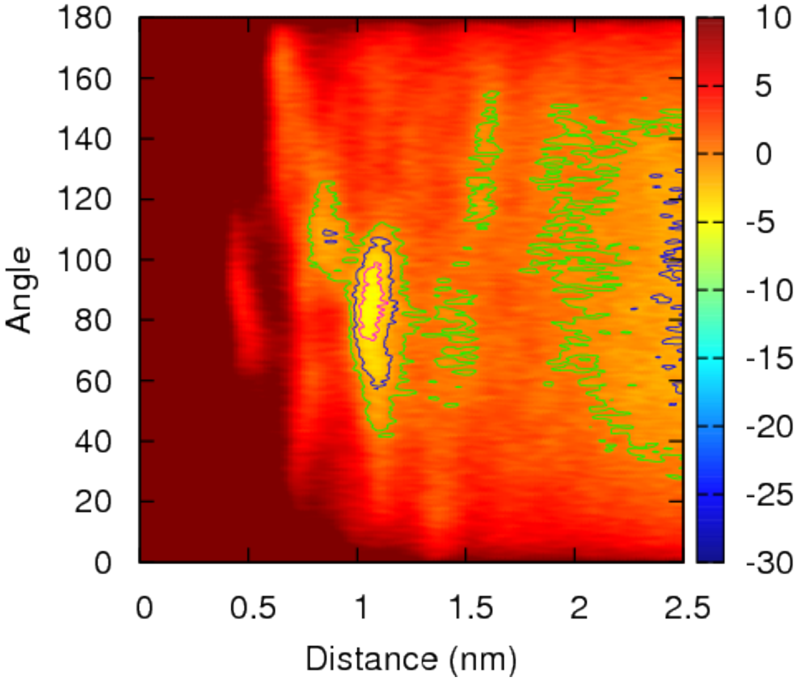

Figure 3-6: Free energy surface for peptide 1b as a function of distance and helix angle in units of kJ/mol. There is only a single shallow minimum in the free energy.

The magnitude of the free energy minima can be quantified from the free energy function, G(r), by evaluating the ratio

$$\frac{\iint_{r=0,\theta=0}^{r=2.5,\theta=180} e^{-\frac{G(r)}{kT}} dr d\theta}{2.5\, nm \cdot 180}$$

Mathematically, this represents the ratio of the average probability per nanometer that the peptides are within a distance of 2.5nm to the probability per nanometer that the peptides are far from each other (where G(r) = 0). For peptide 1b, this ratio is just 0.7 , compared to 100 for peptide 1a. The magnitude of the free energy ratio for peptide 1b is also smaller than for peptide 2b, where the ratio is 1.4, and for peptide 2a, where the probability ratio is 20. The maximum depth of the free energy minimum is 5kJ/mol, or about 2kT. Because the barrier to dissociation is relatively low, it is not a likely candidate to form aggregates.

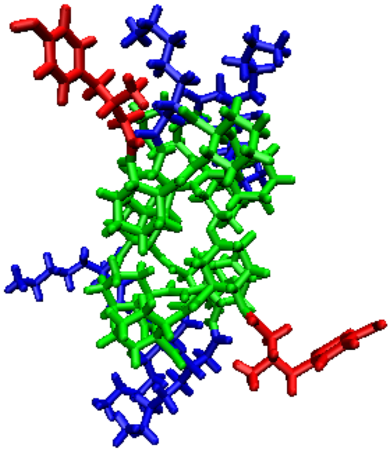

Figure 3-7: Representative configuration of the free energy minimum structure for peptide 1a with the hydrophobic groups facing each other and the end-to-end vectors nearly parallel

Peptides 2a and 2b are the globally amphiphilic and non-globally amphiphilic isomers, respectively, of a β-peptide sequence similar to 1a and 1b, but with three ACHC residues replaced by β_3-homophenylalanine (β^3hPhe). The results for the peptide isomers 2a and 2b, shown in Figures 8 and 9, are surprising at first. The free energy surface for peptide 2a exhibits a free energy minimum that is narrow in the peptide distance parameter, but very wide in the angle parameter. The free energy minima as a function of angle at the free energy minimum distance are very shallow compared to those encountered in peptide 1a (20 kJ/mol for peptide 1a and 8kJ/mol for peptide 2a). The free energy surface for peptide 2b, however, exhibits one deep minimum at about 1.3nm, and the range of the angle parameter is small and that minimum is highly localized at an angular value of 60 degrees. There are two shallower minima at 0.6nm, localized to 60° and 120°. This seems to indicate that the angle is a more significant variable for the non-globally amphiphilic peptide than the globally amphiphilic one, just the opposite result from what was observed for peptides 1a and 1b. This stark difference in behavior is due to the higher degree of conformational freedom of the β^3hPhe residue compared with the cyclic ACHC residues. The ACHC residues have their rings incorporated into the peptide backbone, whereas the β^3hPhe cyclic groups are connected to the backbone by a bond to an intervening carbon atom which is free to rotate. This ability of the hydrophobic phenyl groups to reorient introduces a tolerance for imperfect alignment of the backbones into the free energy surface. Since the phenyl groups can rearrange themselves in order to compensate for changes in the helix angle, the dependence of the free energy on angle is considerably reduced compared to that of peptide 1a.

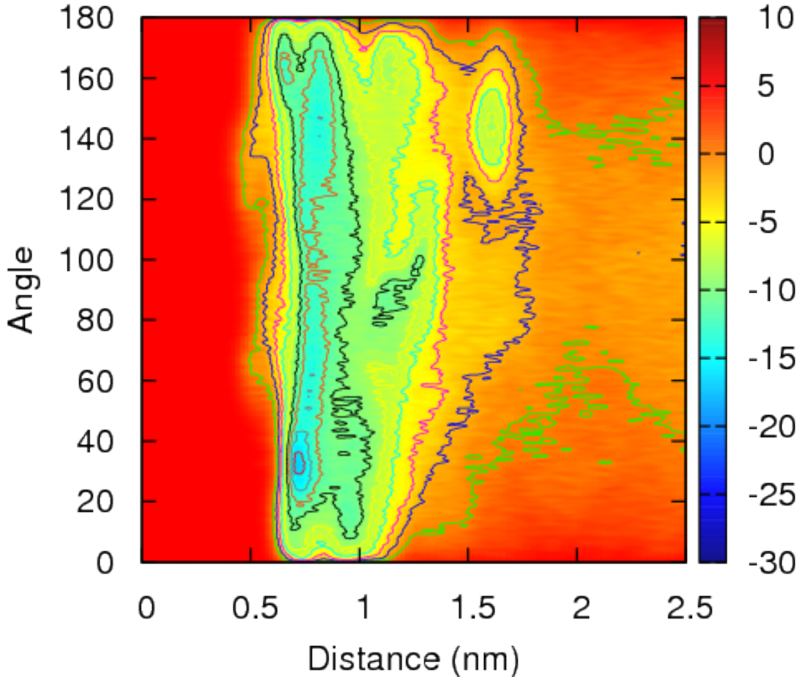

Figure 3-8: Free energy surface for peptide 2a as a function of distance and helix angle in units of kJ/mol. Here the preference for helix angles near 0° or 180° is greatly reduced compared to peptide 1a.

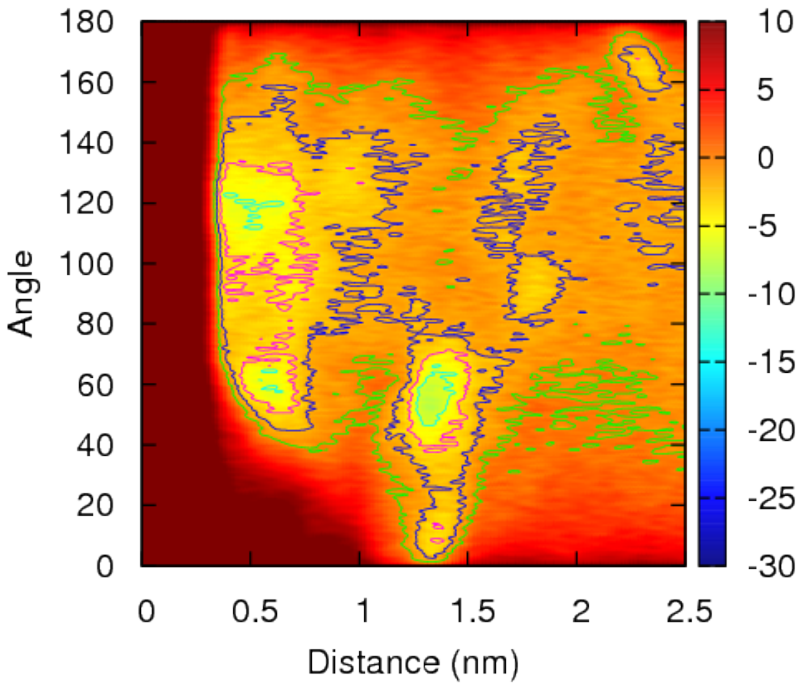

Figure 3-9: Free energy surface for peptide 2b as a function of distance and helix angle in units of kJ/mol. The free energy minimum is significantly deeper than in the case of peptide 1b, and the angular preference is strong.

The situation for the non-globally amphiphilic peptide 2b is also drastically changed from the behavior of the corresponding peptide 1 isomer by the conformational freedom introduced by the β^{3}hPhe residues. Peptide 1b failed to show any deep free energy minima, presumably because no relative orientation of the peptide produces a highly favorable set of interactions. However, with three of the ACHC residues replaced by β^{3}hPhe residues, the hydrophobic groups can rearrange themselves into a favorable configuration, while still presenting the β^3-hLys residues to the solvent. There is a strong, narrow global free minimum corresponding to one configuration that achieves this balance well. A representative frame from this free energy minimum is illustrated in Figure 10. The helices orient with the end-to-end vectors nearly aligned antiparallel, with a slight offset. There is a 60° angle between the helices. The free energy minimum is highly localized at this angle, and slight changes in angle result in steep increases in free energy.

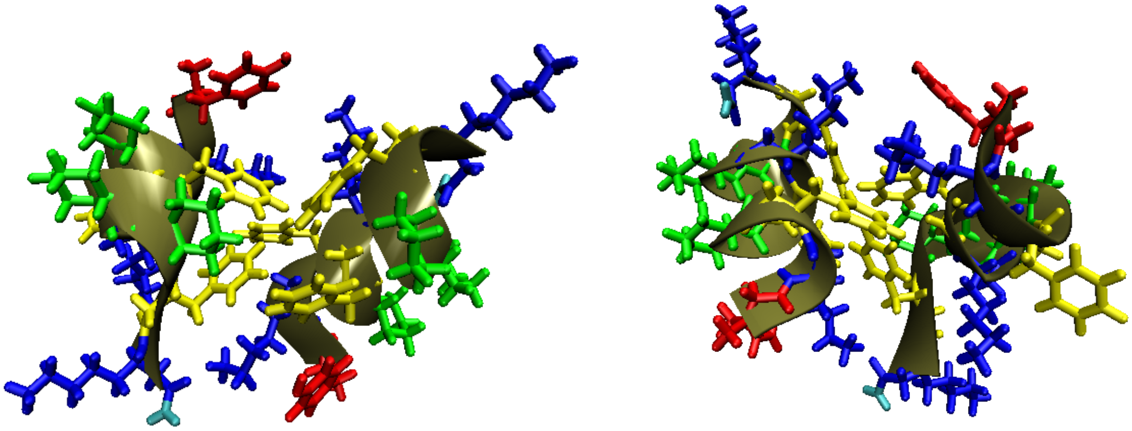

Figure 3-10: Typical frame of the free energy minimum configuration of peptide 2b (right) shown from two angles.

The formation of the anisotropic aggregates proposed by Pomerantz et. al. that lead to the formation of a lyotropic liquid crystal depends on both the propensity for aggregation, and the ability of the mode of aggregation to produce long-range order. Since aggregation with random orientation could not produce long-range order, one would expect liquid crystal formation when aggregation is energetically favorable and the dependence of free energy on orientation is high. This is what is observed in these simulations.

3.4 Comparison of Metadynamics and Constraint Force Methods

The results of two-dimensional simulations using metadynamics show a free energy minimum as a function of distance for all four of the peptides. This result is consistent with the uni-dimensional potentials of mean force by Mondal et al.(15), although some quantitative differences persist.

The free energy from the metadynamics simulations is generally lower at close distances than that generated in short constraint-force calculations. The length of the simulations by Miller et. al. included a brief equilibration of less than 1ns, followed by production runs of 5ns for peptides 1b and 2a, and 10ns for peptides 1a and 2b. A problem with the constraint-force method for molecules of this size is the slow time scale of rotational kinetics at close distances due to stearic effects. To examine these effects, we performed 20ns simulations of peptide 1a using the constraint-force method with the distance constrained to 0.65nm and a uni-dimensional metadynamics simulation starting from the same configuration, and examined the rotational kinetics. Figure 11 shows how the peptide distance and angle vary as a function of time for the metadynamics simulation, while Figure 12 shows the angle as a function of time for the constraint-force simulation.

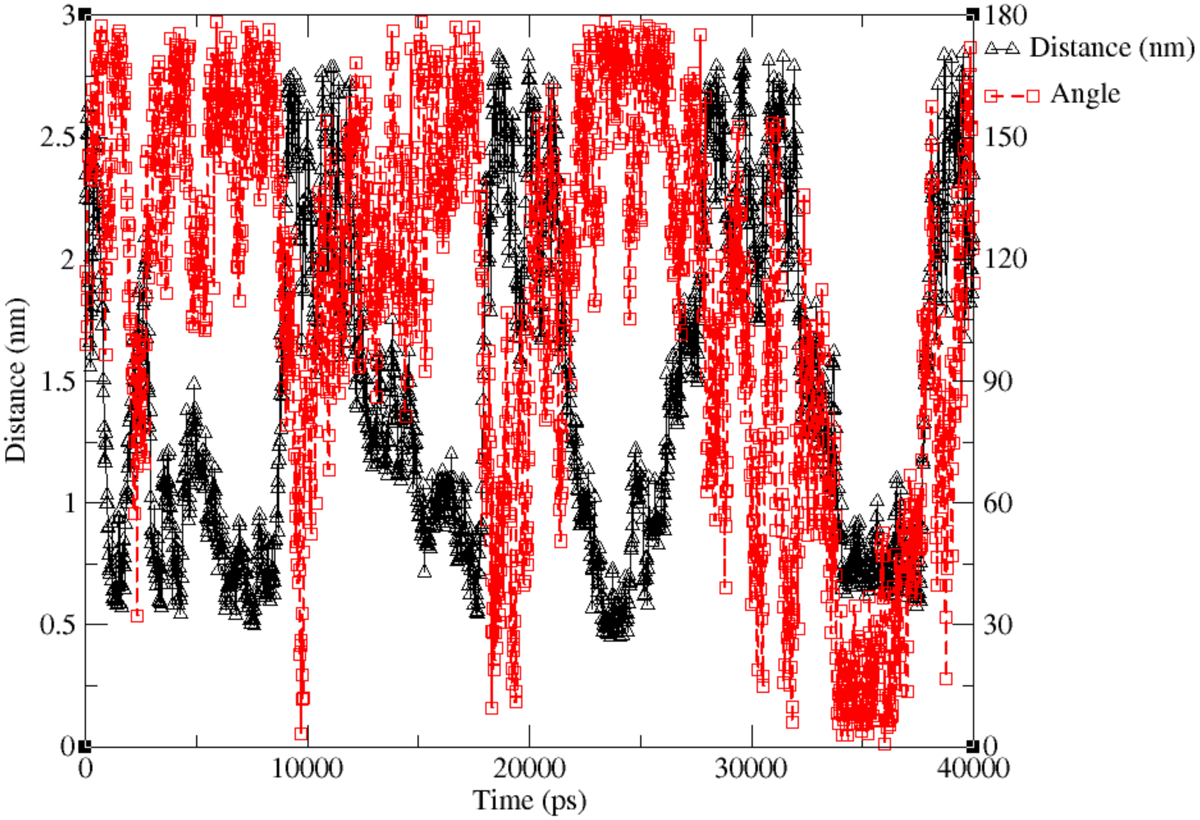

Figure 3-11: Distance and helix angle tracked over 40ns of a metadynamics calculation

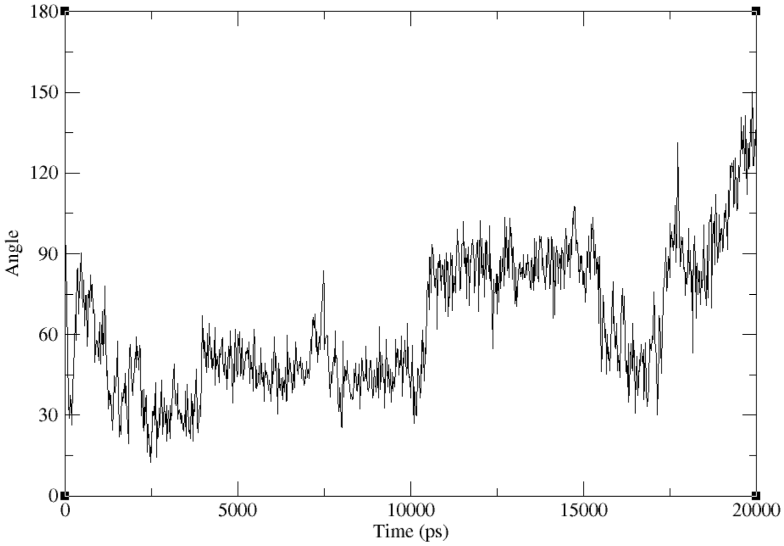

Figure 3-12: Helix angle as a function of time for a 20 ns constraint force simulation

It can be seen that after 10ns the peptide has not undergone a full rotation in the constraint force case, while a wide range of angles is sampled by metadynamics. At the end of the 20ns constraint-force simulation the peptide has transitioned to a higher angle. The slowness of the rotational kinetics at short distances systematically underestimates the free energy at these points. The metadynamics simulations overcome this difficulty by causing the peptides to approach one another along many essentially independent trajectories. In the two-dimensional case the biasing potential ensures that the full range of possible angles is sampled. The umbrella sampling method used by Mondal can mitigate this problem to some extent since the peptides need not remain at very close distances for the entire simulation , but the kinetics of rotation will still be slow when the peptides are close together. Metadynamics leads to enhanced sampling of orientational space, and more reliable results.

3.5 Conclusions

Metadynamics simulations were used to examine the free energy of aggregation of four distinct β-peptides in water. The results of these simulations present a considerable improvement over earlier one-dimensional potentials of mean force generated by earlier simulations.

The free energy surfaces presented here were determined as a function of the separation between molecules and their relative angles. These surfaces provide a more complete understanding of peptide dimerization than that obtained from the one-dimensional potentials of mean force in the literature, including those of our group, and demonstrate that, depending on the sequence of residues along the backbone, β-peptides can exhibit a wide variety of interactions, ranging from only slightly attractive to highly attractive, with sometimes intricate orientational dependencies. Our results are consistent with the predictions of the experimentalists who suggested that highly anisotropic aggregates were responsible for liquid crystal phase behaviour in that peptides that exhibit a very weak attraction or low angular dependence fail to exhibit any liquid crystal phase in experiments. In contrast, peptides that exhibit strong free energy minima and a strong orientational dependence exhibit liquid crystalline behavior and fiber formation in experiments.

This work is supported by the National Science Foundation (NSF) through the Nanoscale Science and Engineering Center (NSEC) at the University of Wisconsin-Madison.

3.6 References

1. Appella, D. H., L. A. Christianson, I. L. Karle, D. R. Powell, and S. H. Gellman. 1996. beta-peptide foldamers: Robust Helix formation in a new family of beta-amino acid oligomers. Journal of the American Chemical Society 118:13071-13072.
2. Daura, X., B. Jaun, D. Seebach, W. F. van Gunsteren, and A. E. Mark. 1998. Reversible peptide folding in solution by molecular dynamics simulation. Journal of Molecular Biology 280:925-932.
3. Daura, X., K. Gademann, B. Jaun, D. Seebach, W. F. van Gunsteren, and A. E. Mark. 1999. Peptide folding: When simulation meets experiment. Angewandte Chemie-International Edition 38:236-240.
4. Miller, C. A., S. H. Gellman, N. L. Abbott, and J. J. de Pablo. 2008. Mechanical stability of helical beta-peptides and a comparison of explicit and implicit solvent models. Biophysical Journal 95:3123-3136.
5. Rathore, N., S. H. Gellman, and J. J. de Pablo. 2006. Thermodynamic stability of beta-peptide helices and the role of cyclic residues. Biophysical Journal 91:3425-3435.
6. Seebach, D., A. K. Beck, and D. J. Bierbaum. 2004. The world of beta- and gamma-peptides comprised of homologated proteinogenic amino acids and other components. Chemistry & Biodiversity 1:1111-1239.
7. Seebach, D., and J. L. Matthews. 1997. beta-peptides: a surprise at every turn. Chemical Communications:2015-2022.
8. Cheng, R. P., S. H. Gellman, and W. F. DeGrado. 2001. beta-peptides: From structure to function. Chemical Reviews 101:3219-3232.
9. Pomerantz, W. C., C. Pizzey, V. Yuwono, S. Paramanov, J. Hartgerink, S. H. Gellman, and N. L. Abbott. 2007. Lyotropic liquid crystals from designed helical beta peptides. John Wiley & Sons Inc. 570-570.
10. Pomerantz, W. C., V. M. Yuwono, C. L. Pizzey, J. D. Hartgerink, N. L. Abbott, and S. H. Gellman. 2008. Nanofibers and lyotropic liquid crystals from a class of self-assembling beta-peptides. Angewandte Chemie-International Edition 47:1241-1244.
11. Pizzey, C. L., W. C. Pomerantz, B. J. Sung, V. M. Yuwono, S. H. Gellman, J. D. Hartgerink, A. Yethiraj, and N. L. Abbott. 2008. Characterization of nanofibers formed by self-assembly of beta-peptide oligomers using small angle x-ray scattering. Journal of Chemical Physics 129:8.
12. Onsager, L. 1949. THE EFFECTS OF SHAPE ON THE INTERACTION OF COLLOIDAL PARTICLES. Annals of the New York Academy of Sciences 51:627-659.
13. Tiddy, G. J. T. 1980. SURFACTANT-WATER LIQUID-CRYSTAL PHASES. Physics Reports-Review Section of Physics Letters 57:1-46.
14. Miller, C. A., S. H. Gellman, N. L. Abbott, and J. J. de Pablo. 2009. Association of Helical beta-Peptides and their Aggregation Behavior from the Potential of Mean Force in Explicit Solvent. Biophysical Journal 96:4349-4362.
15. Mondal, J., X. A. Zhu, Q. A. Cui, and A. Yethiraj. 2010. Self-Assembly of beta-Peptides: Insight from the Pair and Many-Body Free Energy of Association. Journal of Physical Chemistry C 114:13551-13556.

16. Laio, A., and M. Parrinello. 2002. Escaping free-energy minima. Proceedings of the National Academy of Sciences of the United States of America 99:12562-12566.
17. MacKerell, A. D., D. Bashford, M. Bellott, R. L. Dunbrack, J. D. Evanseck, M. J. Field, S. Fischer, J. Gao, H. Guo, S. Ha, D. Joseph-McCarthy, L. Kuchnir, K. Kuczera, F. T. K. Lau, C. Mattos, S. Michnick, T. Ngo, D. T. Nguyen, B. Prodhom, W. E. Reiher, B. Roux, M. Schlenkrich, J. C. Smith, R. Stote, J. Straub, M. Watanabe, J. Wiorkiewicz-Kuczera, D. Yin, and M. Karplus. 1998. All-atom empirical potential for molecular modeling and dynamics studies of proteins. Journal of Physical Chemistry B 102:3586-3616.
18. Jorgensen, W. L., and D. L. Severance. 1990. AROMATIC AROMATIC INTERACTIONS - FREE-ENERGY PROFILES FOR THE BENZENE DIMER IN WATER, CHLOROFORM, AND LIQUID BENZENE. Journal of the American Chemical Society 112:4768-4774.
19. Essmann, U., L. Perera, M. L. Berkowitz, T. Darden, H. Lee, and L. G. Pedersen. 1995. A SMOOTH PARTICLE MESH EWALD METHOD. Journal of Chemical Physics 103:8577-8593.
20. Bussi, G., D. Donadio, and M. Parrinello. 2007. Canonical sampling through velocity rescaling. Journal of Chemical Physics 126:7.
21. Hess, B., C. Kutzner, D. van der Spoel, and E. Lindahl. 2008. GROMACS 4: Algorithms for highly efficient, load-balanced, and scalable molecular simulation. Journal of Chemical Theory and Computation 4:435-447.
22. Bonomi, M., D. Branduardi, G. Bussi, C. Camilloni, D. Provasi, P. Raiteri, D. Donadio, F. Marinelli, F. Pietrucci, R. A. Broglia, and M. Parrinello. 2009. PLUMED: A portable plugin for free-energy calculations with molecular dynamics. Computer Physics Communications 180:1961-1972.
23. Piana, S., and A. Laio. 2007. A bias-exchange approach to protein folding. Journal of Physical Chemistry B 111:4553-4559.
24. Babin, V., C. Roland, and C. Sagui. 2008. Adaptively biased molecular dynamics for free energy calculations. Journal of Chemical Physics 128:7.

Chapter 4: Effect of trehalose on the interaction of human islet amyloid polypeptide with lipid membranes

4.1 Introduction

The formation of fibrous insoluble protein aggregates, or amyloids, is a characteristic of several human diseases. These include Alzheimer's disease(1, 2), Huntington's disease(3), Parkinson's disease(4), and type II diabetes(5). In each of these cases, amyloidogenic peptides nucleate first into oligomers, and then proceed to form fibrils. Although it is amyloid fibrils that are readily observed in damaged cells, there is evidence that these fibrils themselves are not the primary cause of cell damage, but that the oligomers which precede amyloid fibril formation are the toxic species. Cell damage can be brought about in vitro(6, 7), and disease symptoms induced in rat models(8) by the introduction of these soluble oligomers before they form fibrils. This makes the early stages of aggregate formation most important to understanding and preventing the onset of disease.

In the case of diabetes, the amyloid fibrils are composed of human islet amyloid polypeptide (hIAPP), a peptide hormone co-secreted with insulin in the islets of Langerhans by pancreatic β-cells. The formation of these aggregates has been found to be greatly accelerated by the presence of phospholipid membranes, especially anionic phospholipid membranes(7, 9-11). This behavior has been attributed to the fact that membranes provide an environment that facilitates peptide enrichment, reduces the electrostatic repulsion between charged monomers, and destabilizes the peptide's native structure, leading to conformational changes that facilitate the formation of aggregates(11, 12)

hIAPP has a disordered structure in solution, while mature fibrils are known to have a highly β-sheet rich structure. In spite of this, the phospholipid catalyzed formation of amyloid fibrils is preceded the presence of highly α-helical peptide structures(7, 13). The reasons for this are not well understood.

Given the ubiquity of amyloid fibrils in many human diseases, multiple strategies have been pursued to prevent their formation, including development of peptide aggregation inhibitors. In the case of hIAPP, however, only a few molecules have been considered as possible inhibitors of aggregation and cytotoxicity. Among these, resveratrol(14-16), Congo red(17), and phenol red(18) have proved to inhibit both hIAPP fibril formation and the associated cytotoxic effects. It has also been shown that rifampicin and some quinone derivatives inhibit the toxicity of aggregated peptides(19), and that rifampicin and Congo red inhibit membrane activity of non fibrillar hIAPP(20). More recently, two small-molecule rhodanine-scaffold based inhibitors have proved to reduce IAPP fibril formation(21). Trehalose, a disaccharide of glucose, has been shown to inhibit the aggregation of amyloid-β-peptide(22, 23), insulin(24) and polyglutamine peptides(25) in bulk solution. Trehalose has also been shown to interact with the phospholipid headgroups of bilayers membranes(26) and has often been used as a cryoproteotant(27, 28). Given this body of work, it is of interest to consider whether trehalose also influences the aggregation of hlAPP, and its propensity to form aggregates in the presence of negatively charged lipid monolayers and bilayer membranes (in vesicles).

In this work we use simulations and experiments to examine how trehalose effects the interaction of hIAPP with membranes.

4.2 Simulation Methods

In order to study the effect of trehalose on the interaction of hIAPP with lipid monolyaers, we will simulate systems that consist of two DPPG monolayers separated by a layer of solvent containing an hIAPP molecule between the headgroups, and vacuum between the tail groups, as shown in the figure below:

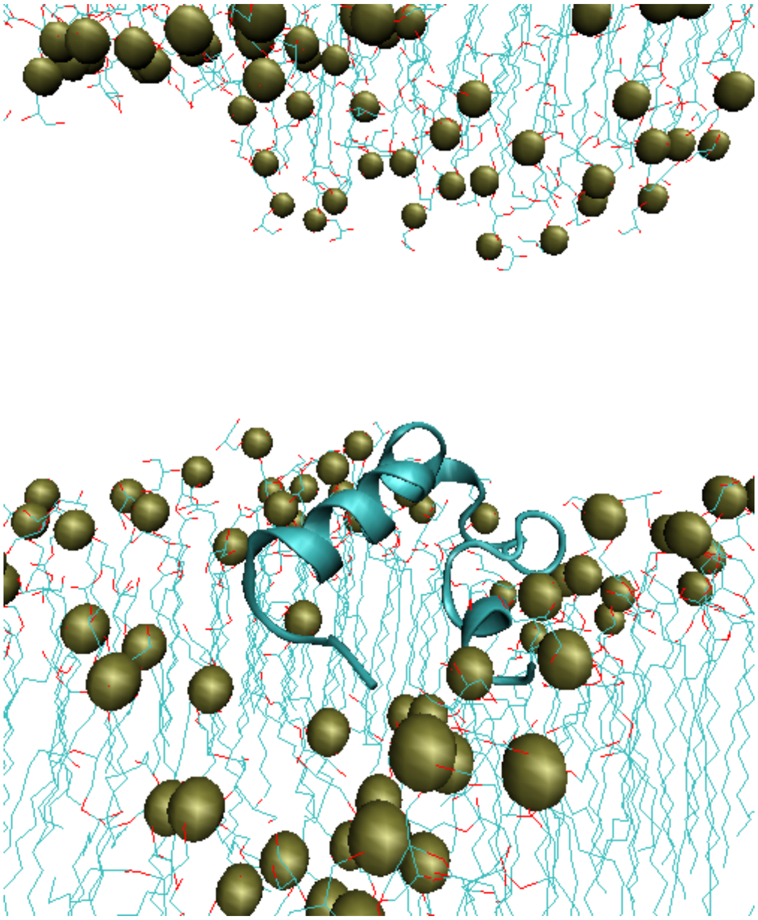

Figure 4-1: System to be simulated with explicit solvent not shown for clarity

Because of the observed increase in a-helical character prior to the formation of aggregates, the effect of trehalose on the α-helicity of hIAPP in the presence of a membrane is of great interest. To accurately simulate these effects, enhanced sampling techniques will be required to speed up transitions between states separated by large energy barriers. As we have seen earlier, metadynamics is one such technique. However, metadynamics has certain drawbacks for this system compared to other methods.

The length of time required for convergence increases rapidly with the number of dimensions of the free energy surface. For collective variables with Gaussian width s and total length L, the time to fill in the free energy surface is proportional to $(L/s)^2$. Because of this, unnecessary collective variable should be avoided. However, a problem arises when the a-helix parameter is sampled in one dimension. When the protein is completely unfolded, the value of the α-helix character gets very close to 0, and no small change in conformation can cause it to increase significantly. This causes the bias to accumulate extremely rapidly in a small region while the reaction coordinate no longer diffuses. As shown in the figure below, there are a wide variety of states to explore in a small region around the value of 0. Much of the free energy calculated depends on the length of these short visits to the boundary. This effect is greatly reduced by the presence of a second dimension in which the states where α-helix character are close to 0 form a line rather than a point. Since introducing a second dimension in the free energy surface increases the computation time greatly, other methods will likely be more efficient.

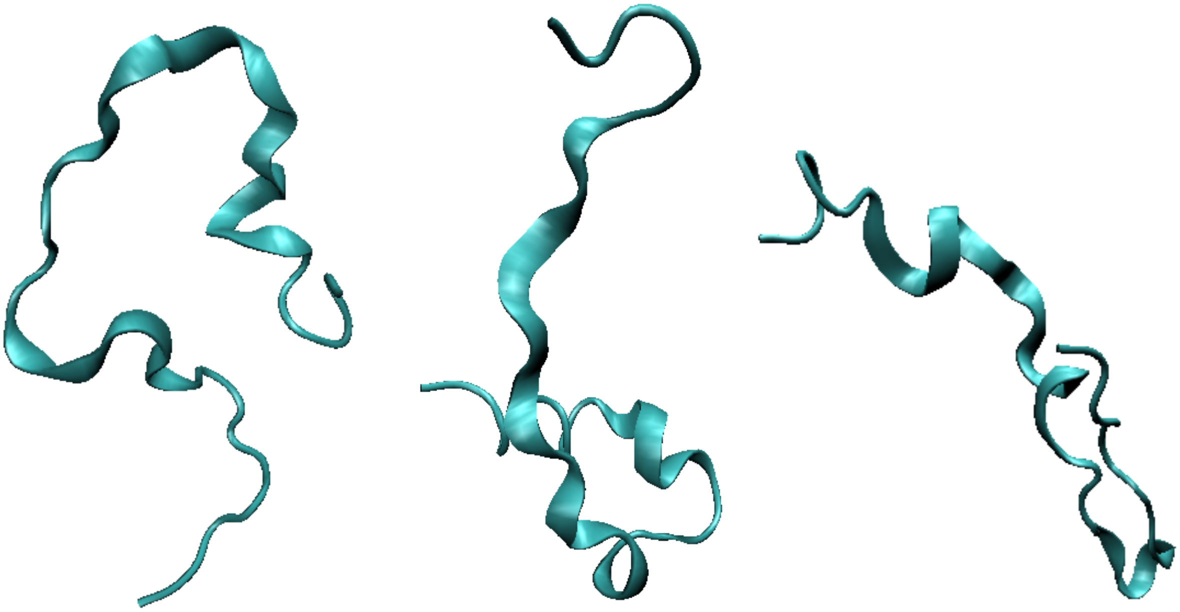

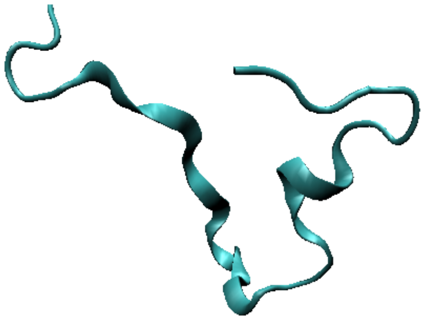

Figure 4-2: Examples of distinct conformations with zero α-helix content

Replica exchange methods allow for enhanced equilibrium sampling of protein conformations and do not suffer from the problems that result from an adaptive bias when much of the conformational space is collapsed to a point. Furthermore, much less of the simulation time is spent exploring physically irrelevant states.

In replica exchange methods, multiple versions of the simulation system are prepared. Each one is simulated under different conditions, such as different temperatures or modified Hamiltonians(29). One simulation box contains the system of interest, while the others contain systems that cross energy barriers more quickly than the system of interest. Periodically, swaps between the configurations are proposed (i.e. interchanging the coordinates between replicas under different conditions), and accepted with a probability that causes detailed balance to be maintained in each simulation box, given by

$$\min\,(1, \beta_m\big(E_m(X_n) - E_m(X_m)\big) - \beta_n\big(E_n(X_m) - E_n(X_n)\big))$$

Where in the initial state, each box i has coordinates X_i and energy function E_i. When temperature is varied between replicas, the probability of acceptance is inversely proportional to the fluctuations in the energy, which in turn are proportional to the square root of the heat capacity and system size. Maintaining a significant probability of acceptance for large systems therefore requires many closely spaced replicas. Since the protein-membrane system is large, this is undesirable.

To overcome this limitation a variation of replica exchange called Replica exchange with solute tempering (REST) has been proposed(30). In this method the Hamiltonian is modified for the protein-protein interactions and for the protein-non-protein interactions, but not for the interactions that don't involve the protein. This effectively increases the sampling of the conformational space of the protein while the number of replicas needed is independent of system size. This is the method we have chosen to adopt for analysis of the structure of the protein.

4.3 Choice of Force Fields

Many force fields exist to simulate protein structures. In the past these force fields were usually parameterized to agree with experimental measurements of the dihedral angle distributions of small peptides or to give the correct secondary structure for highly structured peptides. Advances in computational hardware and techniques have increasingly allowed for accurate simulations of larger peptides with more weakly defined secondary structures. It has been found that many force fields generally give results in poor agreement with experiment for such systems(31). Care must be taken in choosing a force field.

We performed an analysis of several force fields using the version of Islet Amyloid polypeptide found in rats (rIAPP) for which NMR data was available using metadynamics simulations as a function of both α-helix and β-sheet character. Substantial differences were found among force fields in common use. Below are free energy maps for rIAPP for the OPLS, GROMOS53a6, CHARMM27, CHARMM22*, Amberff03w and Amber99sb*ILDN force fields.

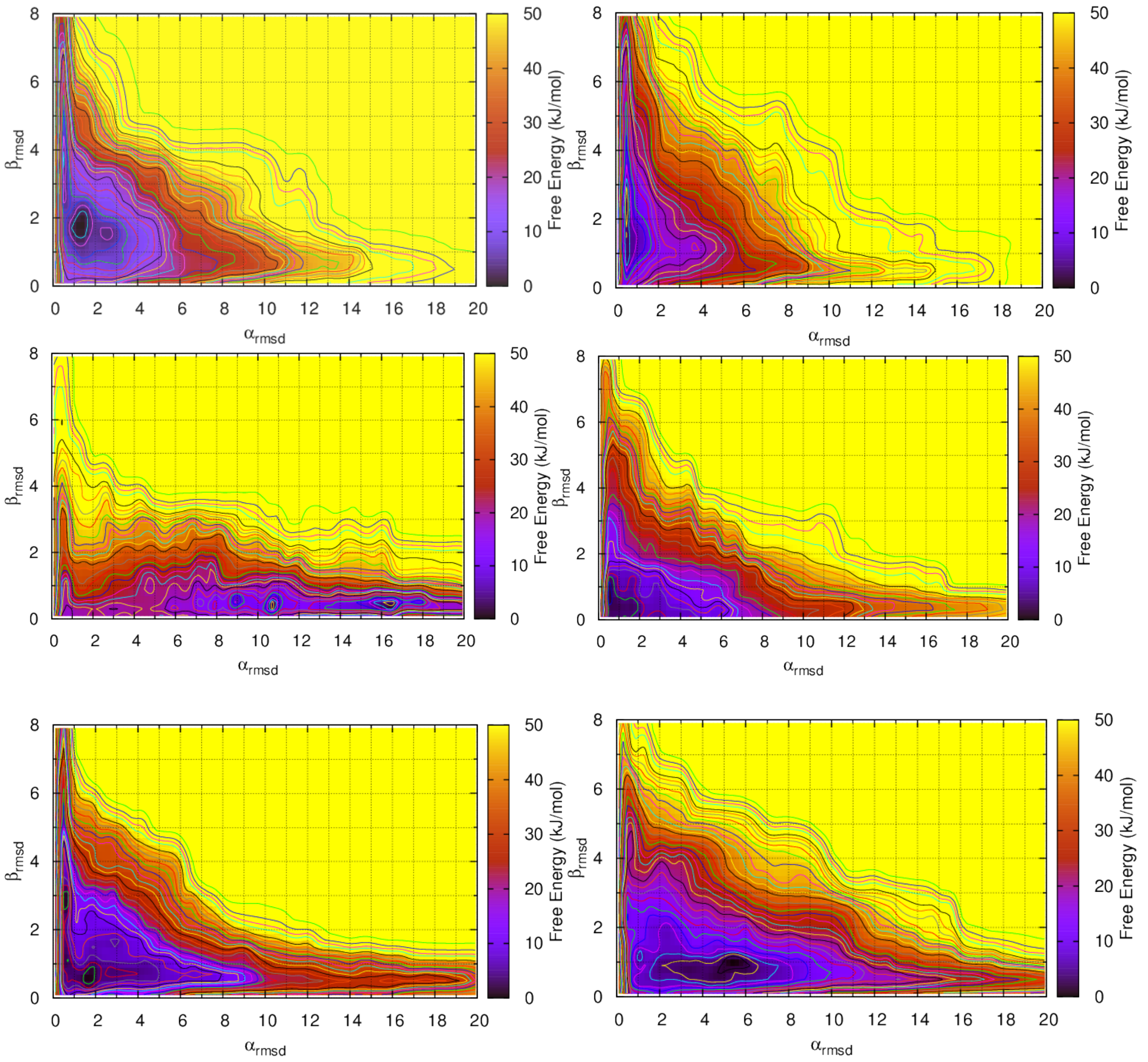

Figure 4-3: Free energy surfaces from metadynamics simulations of rIAPP in water as a function of α-helix and β-sheet character. The force fields are, clockwise from the top left: OPLS, GROMOS53a6, CHARMM22*, Amber99sb*ILDN, Amberff03w, and CHARMM27

Notice that compared to the other force fields, CHARMM27 has a strong α-helical bias, while GROMOS53a6 has a strong β-sheet bias. These force fields were only parameterized using short or strongly structured peptides. CHARMM22*, Amber99sb*ILDN and Amberff03w were all parameterized against weakly structured peptides. They show much better agreement with the NMR data shown in the figure below prepared by Kyle Hoffman.

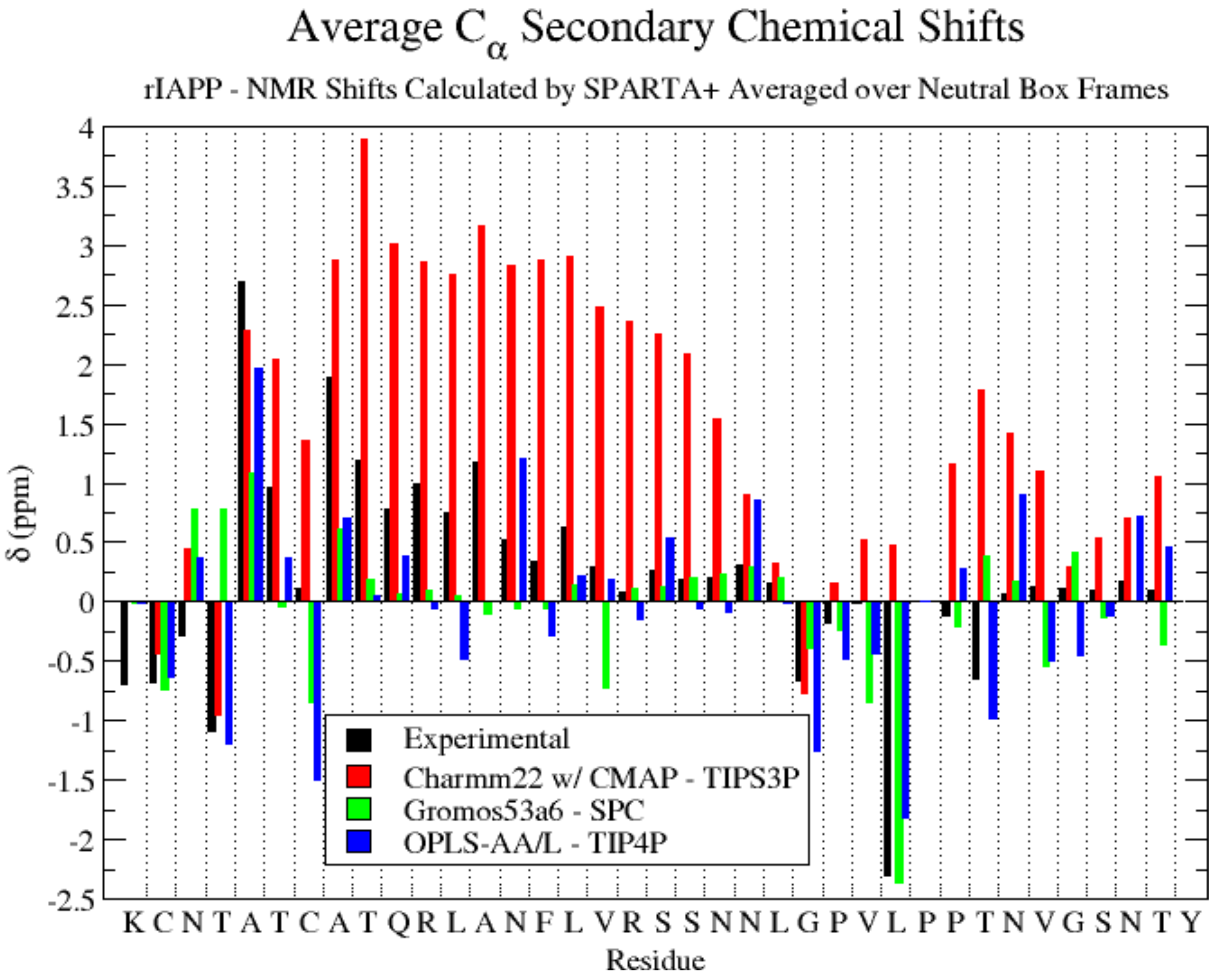

Figure 4-4: Comparison of experimental NMR shift data to predictions from simulations for CHARMM22, GROMOS53a6 and OPLS

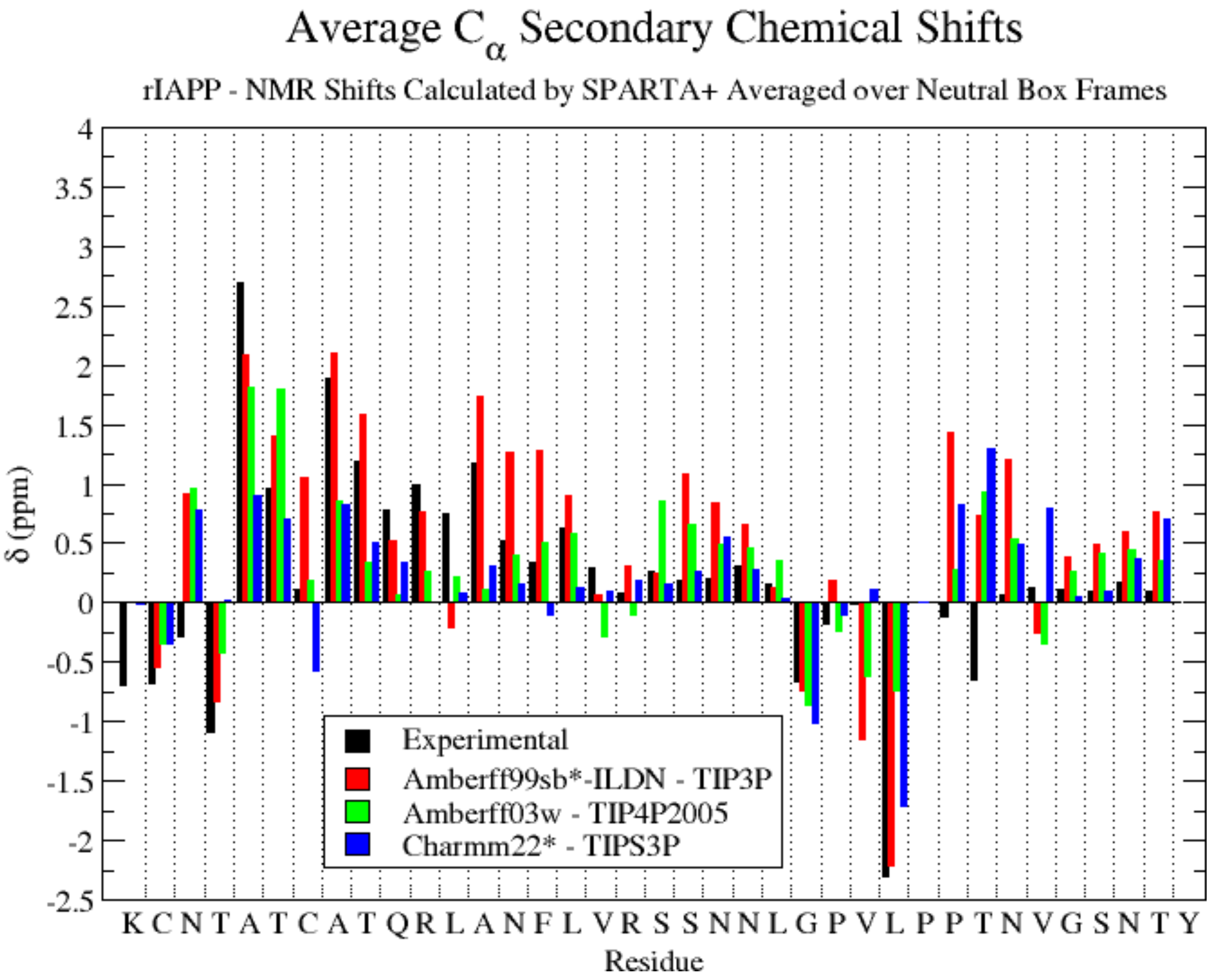

Figure 4-5: Comparison of experimental NMR shift data to predictions from simulations for Amber99sb*ILDN, Amberff03w, and CHARMM22*

The force fields that were parameterized using weakly structured peptides match the experimental predictions much more closely. In this work, we use CHARMM36 which was parameterized in a similar manner to CHARMM22* to give accurate results for weakly structured peptides, and also includes a lipid force field.

4.4 Simulation Details

Simulations were performed for DPPG monolayer systems with and without trehalose, in the presence of hIAPP peptide. The initial structure of the DPPG monolayer was taken from an equilibrated DPPC membrane structure consisting of 128 lipids (32), and the headgroups were modified to produce a DPPG monolayer. The system consisted of two monolayers with 64 lipids each with a layer of solvent between them, and vacuum on the outside. In each case there were approximately 4500 TIP3P water molecules, as well as sodium counter-ions to preserve electroneutrality. Trehalose systems contained 25 molecules of trehalose.

The system then underwent simulated annealing, with the system starting at a temperature of 450K for 20ns, and then cooling down at a linear rate to 300K. The surface tension was held constant at 25 mN/m using the Berendsen barostat. In all simulations, the temperature was coupled with the velocity rescaling thermostat(33) using a temperature coupling parameter of 0.002ps. A particle-mesh Ewald sum was used for long-range electrostatic interactions with a short range cut-off of 10 Å and a maximum relative error of 10-5(34). A cut-off of 10 Å was also used for Lennard-Jones interactions. Bonds were constrained with the LINCS algorithm, and a time step of 0.002 ps was used. The simulations were performed using the gromacs (35) simulation package.

The final structures obtained from the annealing simulations of the monolayers were used to generate configurations containing the peptide. The InflateGRO methodology was used to insert the peptide into the simulation box(36). In this method, the solvent is removed, then the lipids positions are dilated. The peptide is inserted, and then restored to its original size through a series of contractions and energy minimizations. It is finally resolvated after this, and equilibrated for 5ns. Surface tension vs. Area isotherms were generated to find the surface tension that corresponds best to experimental conditions by running 12ns simulations at surface tension ranging from 0 to 35mN/m. Surface tension is related to surface pressure by

$$P = \gamma_{water} - \gamma$$

Since the surface tension of water of the TIP3P water model is not exactly the same as the experimental value, and depends somewhat on film thickness, we generate a surface pressure-area isotherm and match to the experimental conditions based on the shape of the curve. Based on this data, REST simulations were run at a constant surface tension of 35 mN/m. 16 replicas of each system were simulated with effective temperatures ranging from 303.15K to 650K.

4.5 Results

We begin our discussion by presenting results for the effect of trehalose on a DPPG monolayer, and then present our observations for peptide insertion into the negatively charged lipid monolayer. Figure 4-6 shows the compression isotherms of DPPG on water, 100mM trehalose, PBS and PBS with 100mM trehalose subphases at 30°C. The compression isotherms show that the packing density of the lipid is significantly lower on PBS than on the water subphase. It has been reported that, on a buffer subphase, the phosphatidyl glycerol groups of DPPG ionize, leading to increased solvation(37). This ionization might cause changes in the orientation of the polar groups, and conformational changes upon compression(37). As can be seen in Figure 4-6, adding trehalose causes the lipid to be more loosely packed. Note that the "expanding" effect of trehalose is more pronounced for the monolayer on a water subphase than on PBS (Figure 4-6). Our experimental results for DPPG isotherms on pure water(38, 39) and on 100mM trehalose aqueous solution(38) are consistent with literature reports, and serve to validate our experimental procedures. Lambruschini and coworkers(40) reported compression isotherms of DPPC monolayers on water and 100 mM trehalose subphases at 22°C, and also observed an expansion in the monolayer area upon addition of trehalose. DPPG isotherms on PBS subphases have only been reported at 21°C, and thus cannot be directly compared to our data(41, 42).

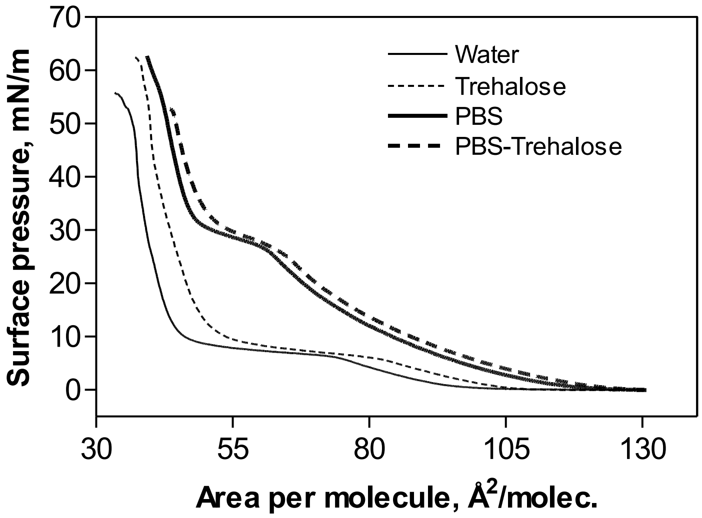

Figure 4-6: Compression isotherms of DPPG on water, 100 mM trehalose, PBS and PBS/100mM trehalose subphases at 30°C.

The surface pressure-area isotherms from the simulations in Figure 4-7 show a similar trend, with trehalose expanding the membrane at high surface tension, although this trend does not hold at low surface tension. The simulation system uses fully charged lipids, which correspond to the experimental condition where PBS is present.

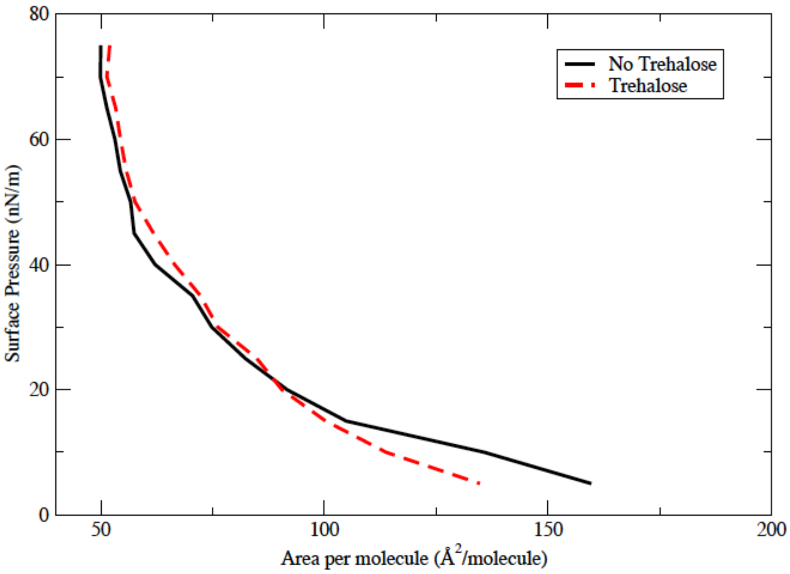

Figure 4-7: -Surface tension vs. area isotherm for hIAPP-DPPG system with and without trehalose

The interaction of hIAPP with monolayers, which ultimately leads to membrane damage, could consist of peptides adsorbing on the membrane surface or it could involve peptide insertion into the membrane. To examine these possibilities, we performed hIAPP insertion experiments into DPPG monolayers. Our primary aim was to monitor the kinetics of the interaction of the peptide with the monolayer in different subphases (pure water, trehalose, PBS, and PBS/trehalose). For each subphase, a DPPG monolayer was compressed up to 25 mN/m and kept at that surface pressure. The change in the monolayer area after the injection of the peptide into the subphase was then recorded. Figure 4-8 shows the relative change in the monolayer area after peptide injection as a function of time. On all four subphases, the area increase, (caused by peptide insertion) exhibits a sigmoid shape consisting of a lag time, a growth phase and a plateau. The lag time before the peptide starts inserting into the monolayer is not affected by the subphases considered in this study. This observation should be contrasted with results for the insertion of amyloid-b peptide into DPPG monolayers, where the presence of trehalose eliminates the occurrence of a lag time(38). Addition of trehalose causes an increase in the rate of monolayer area expansion. It can also be seen in Figure 4-8 that the overall area change is six to eight times higher on water than on a PBS subphase, although at 25 mN/m the area per lipid molecule is much larger on the PBS subphase (Figure 4-6). Addition of trehalose increases the overall area change, by 20 and 50 percent for the water and PBS subphases, respectively. Similar hIAPP insertion curves have been reported for POPE/POPS or DMPC monolayers at room temperature on pure water surfaces(20). By comparing the insertion of the peptide in monolayers containing negatively charged lipids with the insertion in monolayers containing only zwitterionic lipids, several authors concluded that the interaction of the peptide with the lipid interface is largely determined by electrostatic interactions, as the peptide is only able to associate strongly with negatively charged lipids(43, 44). It has also been shown that the peptide insertion into monolayers is driven by the N-terminal part of the peptide(43, 44).

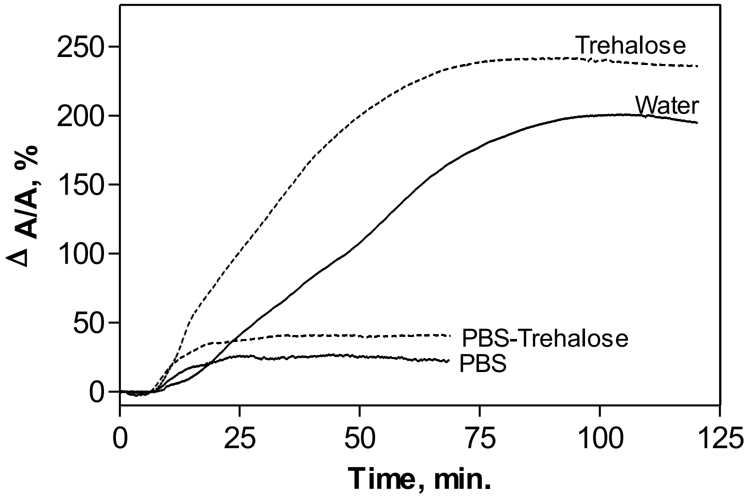

Figure 4-8: Percent area change versus time isotherms of a DPPG film at a constant surface pressure of 25 mN/m after injection of hIAPP into the aqueous subphase at time zero.

The morphological changes of the DPPG monolayer resulting from hIAPP injection were observed with a fluorescence microscope during the insertion process (shown in Figure 4-8). Figure 4-9 and 4-10 show micrographs of the monolayers on PBS (Fig. 4-9a and b), PBS/trehalose (Fig. 4-9 c and d), water (Fig. 4-10 a-c), and trehalose (Fig. 4-10 d-f) subphases before and after peptide injection. On all subphases, the DPPG monolayer exhibits a morphology consisting of dense and expanded domains. The condensed phase is dark, as a result of the exclusion of the large dyed lipid molecules due to stearic impediments. The less ordered, expanded phase exhibits a bright appearance due to preferential segregation of the dye. The insertion of the peptide causes the bright areas to grow. That growth or expansion is attributed to a the disruption of the packing of the lipids in the expanded domains by the peptide(45). Indeed, using dual probe experiments Ege and coworkers showed that the bright areas of the lipid correspond to the areas where the amyloid-β peptide inserts(45). A comparison of Figures 4-9 and 4-10 reveals that the domain morphology is affected by the presence of phosphate buffer. The addition of buffer salts and sugar causes the lipid packing density to be lower than that observed for pure water at 25 mN/m. The higher degree of area expansion observed in the presence of trehalose (Figure 4-8) can also be inferred by comparing the domain morphologies after peptide injection in figures 4-9 and 4-10.

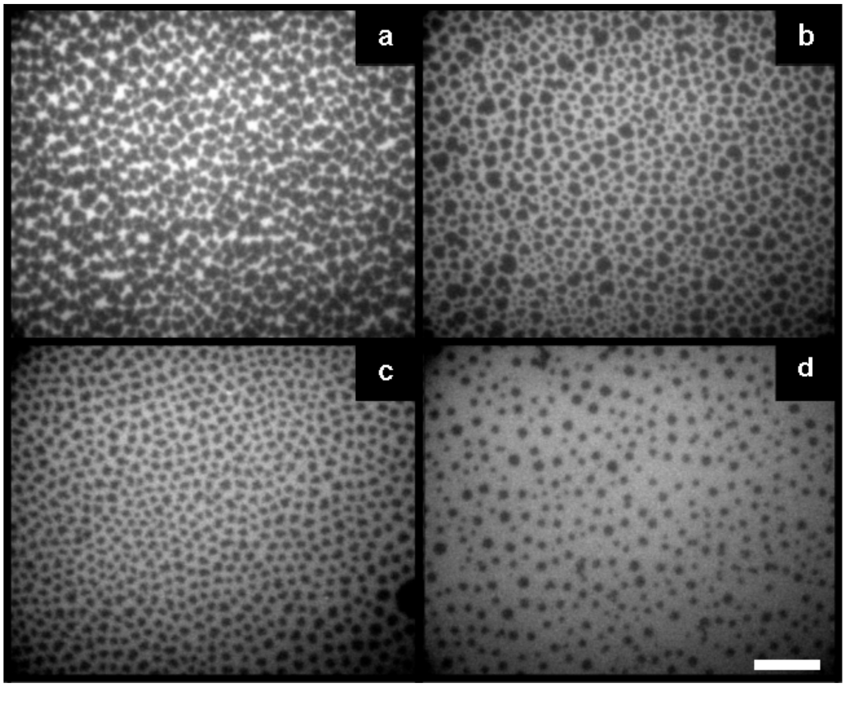

Figure 4-9: Fluorescence micrographs showing the domain morphology of a DPPG monolayer at 30ºC and 25mN/m on (a,b) PBS and (c,d) PBS/trehalose subphases (a,c) before and (b,d) 1 hr after peptide injection into the subphase. The scale bars is 100nm.

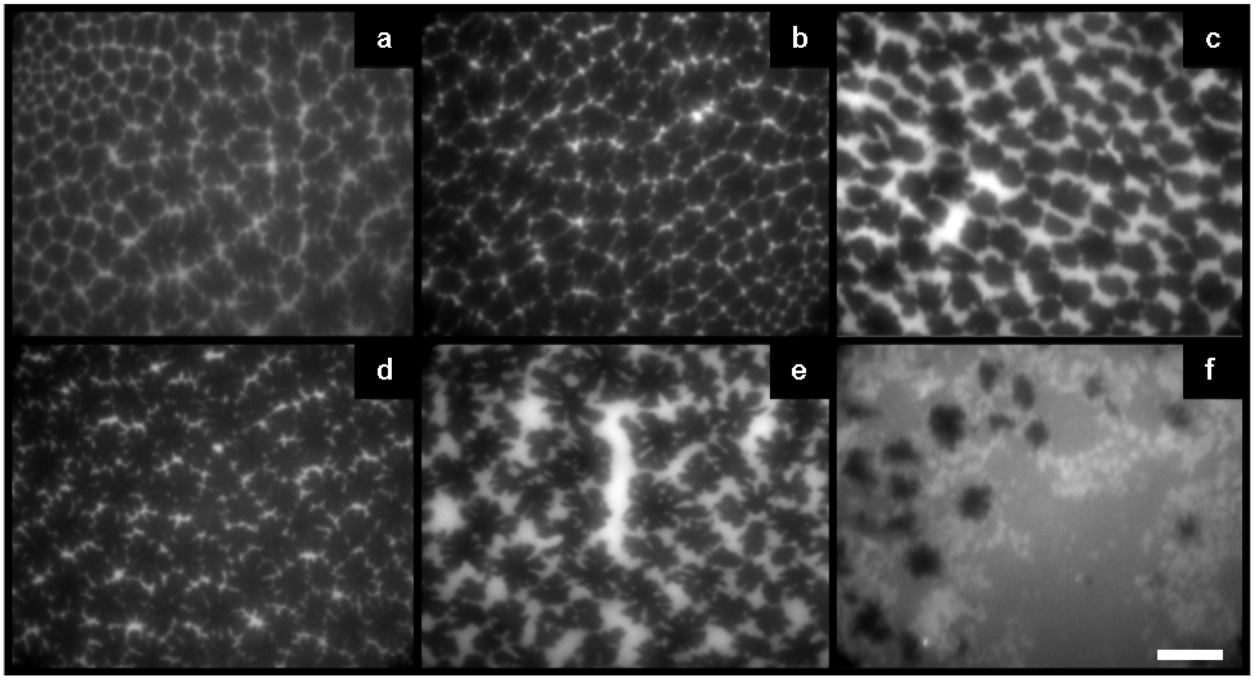

Figure 4-10: Fluorescence micrographs showing the domain morphology of a DPPG monolayer at 30ºC and 25mN/m on (a,b,c) water and (d,e,f) trehalose subphases (a,d) before and (b,e) 30 min after and (c,f) 2 hours after peptide injection into the subphase. The scale bars is 100nm.

In order to gain a better of understanding of the peptide insertion behaviors depicted in Figures 4-6 to 4-10, and to distinguish the effects of the monolayer or bilayer from those of the bulk environment, we now turn our attention to the main kinetic features of hIAPP fibrillogenesis and the influence of solution conditions on that process. Fiber formation was monitored in real time by fluorescence of thioflavin T (Th T), a dye that binds specifically to amyloid structures(46). Figure 4-11 shows the kinetic profile of hlAPP aggregation in the absence or presence of DPPG liposomes. It has been previously reported that these kinetic profiles for fibril formation are characterized by a lag phase and a sigmoidal transition(7, 9-11, 47). PBS containing samples in the absence of liposomes exhibit a long lag time before aggregation begins, which takes from 7 to 10 hours, and the kinetics of aggregation is not affected by the addition of trehalose. These samples reached a plateau after 24 hours of incubation at 30°C (not shown). Similar results have been reported for 10 mM hIAPP in phosphate buffer at room temperature(10, 11). The samples in water or trehalose solution did not aggregate, even after 7 days of incubation at 30°C. Upon the addition of DPPG liposomes, the samples containing PBS aggregate up to 6 times faster than those without the vesicles, and the lag time decreases to about 1 hour (Figure 4-11). Trehalose, added to PBS, causes a 30% increase in the extent of aggregation. In contrast, the samples containing water or trehalose solutions do not exhibit a lag time at the conditions considered in this work; the presence of trehalose had a minimal effect on aggregation. The aggregation values were in those cases much lower than those observed in the presence of PBS.

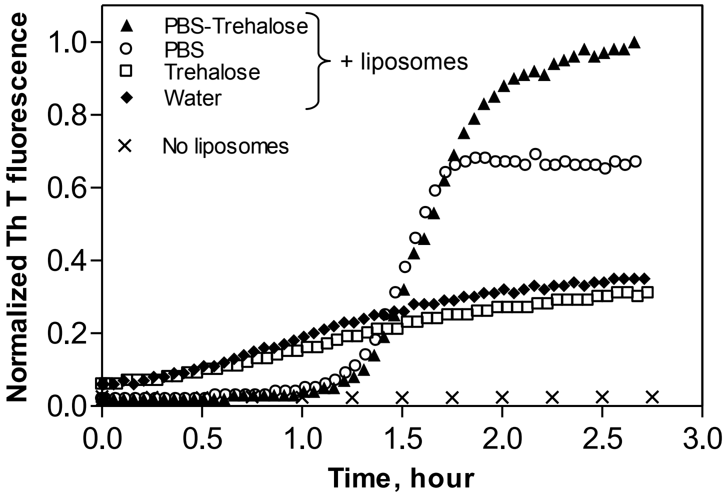

Figure 4-11: hIAPP fiber formation monitored by Thioflavin T (Th T) fluorescence along time at 30°C. All the samples without liposomes (water, trehalose, PBS, PBS/trehalose) gave similar results for the time range shown in this figure (x).

A final question that remains to be addressed is whether the increase aggregation rate induced by trehalose in PBS actually translates into greater bilayer damage or not. While the precise mechanisms and structures that cause membranes to leak remain unclear, there are at least three structurally divergent modes that may account for this fact: the binding of prefibrilar states on the membrane (carpeting), the formation of holes by removal of lipids (detergent effect), and the formation of pores(48). Figure 4-12 shows results for the leakage of dye from calcein filled DPPG large unilamellar vesicles upon addition of hIAPP. The leakage curves are characterized by exponential kinetic profiles; it can be observed that trehalose causes at least 30% increase in leakage. Several authors have reported results from leakage experiments using different lipid and buffer compositions(7, 9, 13). Binding studies suggest that hIAPP peptides bind lipids in a monodisperse fashion(43) and then form alpha-helical aggregates(13). Leakage occurs when α-helical states are significantly populated(13).

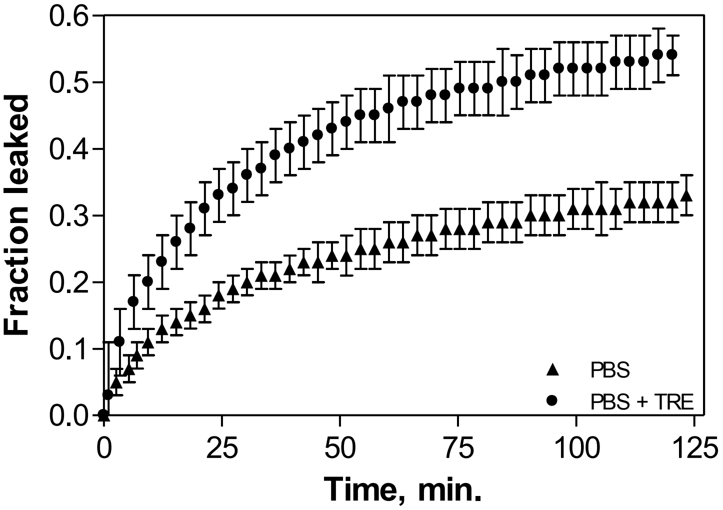

Figure 4-12: Calcein leakage from DPPG large unilamellar vesicles induced by hIAPP. Each experiment was repeated three times; the average and the standard deviation are shown. All experiments were performed in PBS, pH 7.4 at 30°C.

Because the peptide structures that correspond with membrane damage are α-helical, it is of interest to examine the secondary structure of the peptide under various conditions. Simulations were carried out to examine the structure of the peptide under different conditions. Secondary structure time series from the REST simulations of hIAPP in bulk solutions with different concentrations of trehalose are presented in Figure 4-13. We see that trehalose strongly promotes a-helical states in the bulk phase, especially in the region between residues 20 and 27.

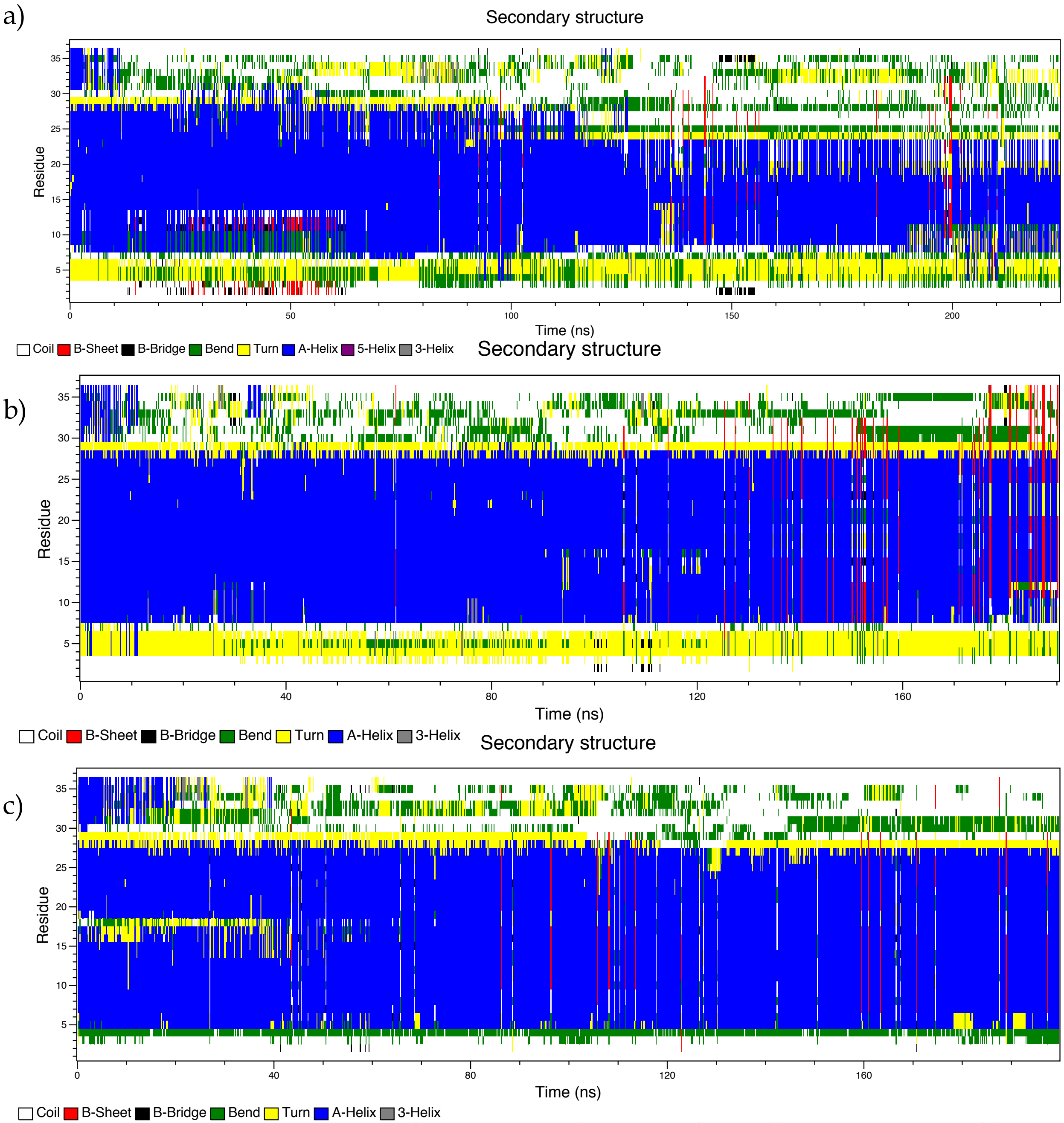

Figure 4-13: Secondary structure vs. time for hIAPP in a bulk solution of water(a), 100mM trehalose (b), and 200mM trehalose (c). α-helix is in blue

REST simulations were also carried out for hIAPP in the presence DPPG membranes. The results for the secondary structure are shown in Figure 4-14.

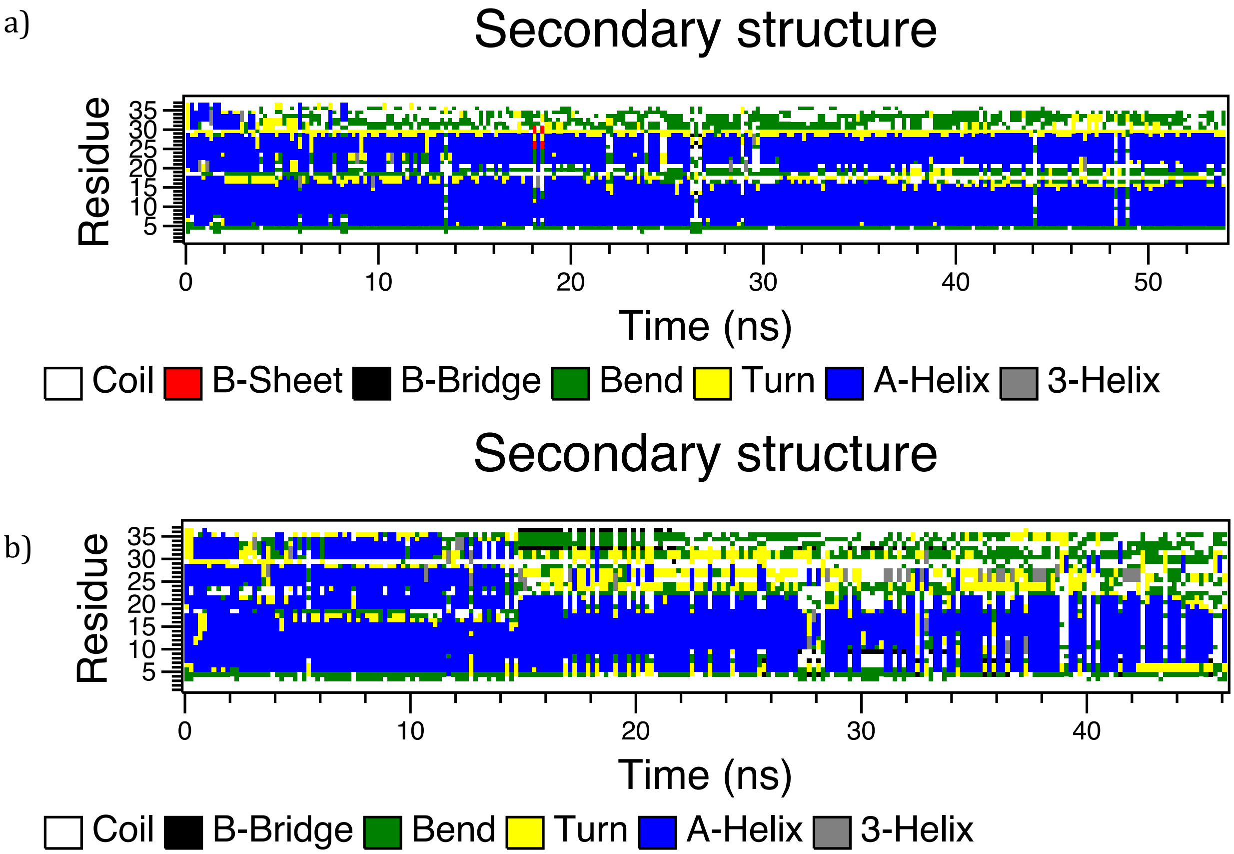

Figure 4-14: hIAPP secondary structure vs. time in the presence of a DPPG monolayer solvated in (a) water and (b) water and trehalose.

In the presence of the DPPG monolayer, trehalose does not increase the stability of the α-helix, and the average number of a-helical residues is actually slightly less. As shown in Figure 4-15, the peptide in the solvent with no trehalose has a turn region around residue 20 separating two α-helical domains, while in the presence of trehalose one of these regions, the region from 20-27 is no longer α-helical, while the turn region is now α-helical.

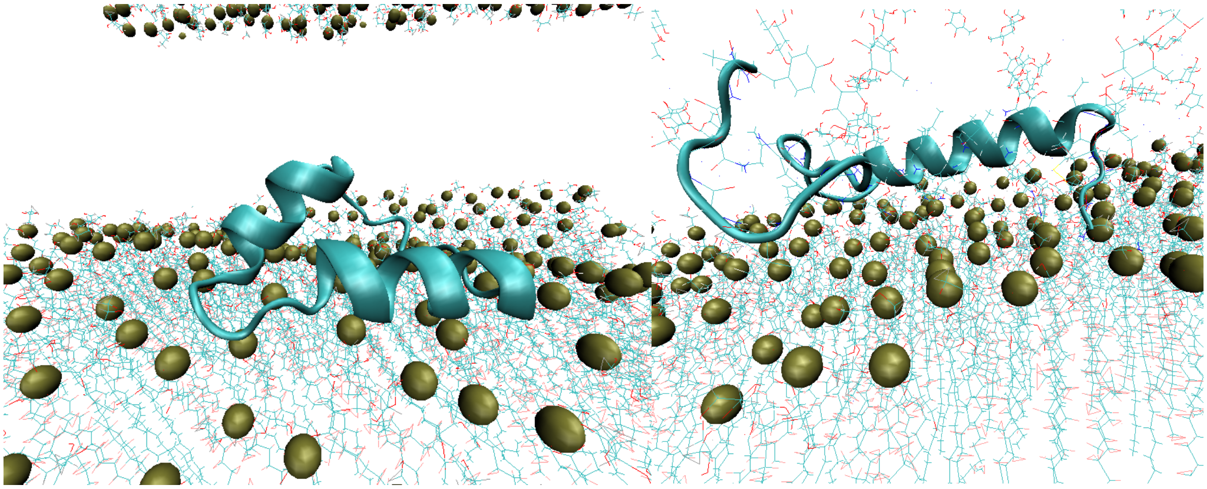

Figure 4-15: Representative frames from REST simulations of hIAPP in the presence of a DPPG monolayer and solvated in water (left) and water/trehalose (right).

Table 4.1 shows the average level of α-helix content for the five systems.

Table 4.1: Average α-helix content of five systems

System:	**Water**	**100mM Trehalose**	**200mM Trehalose**	**Water with DPPG lipid**	**Water/Trehalose with DPPG**
Average α-helix content	**46%**	**53%**	**59%**	**51%**	**46%**

4.6 Discussion

We have seen that trehalose, regardless of the presence of PBS, increases the area of the lipid membrane (Figure 4-6)increases insertion of hIAPP into the membrane (Figure 4-8),increases amyloid fibril formation (Figure 4-11), and increases permeabilization of the membrane (Figure 4-12). Because soluble oligomers of hIAPP are believed to cause membrane damage and later grow into fibrils, this suggests that trehalose increases the rate of formation of oligomers in the presence of membranes. Circular dichroism experiments have shown that hIAPP dissolved in water adopts a random coil conformation and, upon addition of phospholipid vesicles, it adopts a predominant α-helical structure that within minutes converts into a β-sheet conformation, which is consistent with the formation of fibers(7,10,11,13). Our simulations show that α-helical secondary structures are stabilized in bulk solution, but not near the membrane, by trehalose.

A plausible explanation for this is that by stabilizing the α-helix in the bulk phase, trehalose causes the peptides to adopt a conformation more similar to the oligomers as they arrive at the membrane. The negatively charged membrane serves to enrich the local peptide concentration by attracting peptides(50). Oligomer formation likely occurs at the membrane surface itself, and the stable conformations of oligomers at the interface are not necessarily the same as the stable conformations of monomers at the interface.

It is instructive to note that the effect of trehalose on the secondary structure and stabilization of a peptide is molecule specific. The insertion of amyloid-β peptide into DPPG monolayers at 30°C, for example, exhibits a distinct lag time of 20 minutes in pure water, which disappears with the addition of 100mM trehalose(38). In contrast, the results presented in this work show that the lag time before hIAPP insertion into DPPG monolayers (under the same conditions) is 6 minutes on a water subphase, and is not affected by the addition of 100mM trehalose

4.6 References

1. Caughey, B., and P. T. Lansbury. 2003. Protofibrils, pores, fibrils, and neurodegeneration: Separating the responsible protein aggregates from the innocent bystanders. Annual Review of Neuroscience 26:267-298.
2. Soto, C. 2003. Unfolding the role of protein misfolding in neurodegenerative diseases. Nature Reviews Neuroscience 4:49-60.
3. Scherzinger, E., R. Lurz, M. Turmaine, L. Mangiarini, B. Hollenbach, R. Hasenbank, G. P. Bates, S. W. Davies, H. Lehrach, and E. E. Wanker. 1997. Huntingtin-encoded polyglutamine expansions form amyloid-like protein aggregates in vitro and in vivo. Cell 90:549-558.
4. Wood, S. J., J. Wypych, S. Steavenson, J. C. Louis, M. Citron, and A. L. Biere. 1999. alpha-synuclein fibrillogenesis is nucleation-dependent - Implications for the pathogenesis of Parkinson's disease. Journal of Biological Chemistry 274:19509-19512.
5. Hull, R. L., G. T. Westermark, P. Westermark, and S. E. Kahn. 2004. Islet amyloid: A critical entity in the pathogenesis of type 2 diabetes. Journal of Clinical Endocrinology & Metabolism 89:3629-3643.
6. Janson, J., R. H. Ashley, D. Harrison, S. McIntyre, and P. C. Butler. 1999. The mechanism of islet amyloid polypeptide toxicity is membrane disruption by intermediate-sized toxic amyloid particles. Diabetes 48:491-498.
7. Brender, J. R., E. L. Lee, M. A. Cavitt, A. Gafni, D. G. Steel, and A. Ramamoorthy. 2008. Amyloid fiber formation and membrane disruption are separate processes localized in two distinct regions of IAPP, the type-2-diabetes-related peptide. Journal of the American Chemical Society 130:6424-6429.
8. Lesne, S., M. T. Koh, L. Kotilinek, R. Kayed, C. G. Glabe, A. Yang, M. Gallagher, and K. H. Ashe. 2006. A specific amyloid-beta protein assembly in the brain impairs memory. Nature 440:352-357.
9. Engel, M. F. M., L. Khemtemourian, C. C. Kleijer, H. J. D. Meeldijk, J. Jacobs, A. J. Verkleij, B. de Kruijff, J. A. Killian, and J. W. M. Hoeppener. 2008. Membrane damage by human islet amyloid polypeptide through fibril growth at the membrane. Proceedings of the National Academy of Sciences of the United States of America 105:6033-6038.
10. Jayasinghe, S. A., and R. Langen. 2005. Lipid membranes modulate the structure of islet amyloid polypeptide. Biochemistry 44:12113-12119.
11. Knight, J. D., and A. D. Miranker. 2004. Phospholipid catalysis of diabetic amyloid assembly. Journal of Molecular Biology 341:1175-1187.
12. Gorbenko, G. P., and P. K. J. Kinnunen. 2006. The role of lipid-protein interactions in amyloid-type protein fibril formation. Chemistry and Physics of Lipids 141:72-82.
13. Knight, J. D., J. A. Hebda, and A. D. Miranker. 2006. Conserved and cooperative assembly of membrane-bound alpha-helical states of islet amyloid polypeptide. Biochemistry 45:9496-9508.
14. Evers, F., C. Jeworrek, S. Tiemeyer, K. Weise, D. Sellin, M. Paulus, B. Struth, M. Tolan, and R. Winter. 2009. Elucidating the Mechanism of Lipid Membrane-Induced IAPP Fibrillogenesis and Its Inhibition by the Red Wine Compound Resveratrol: A

Synchrotron X-ray Reflectivity Study. Journal of the American Chemical Society 131:9516-9521.

15. Mishra, R., D. Sellin, D. Radovan, A. Gohlke, and R. Winter. 2009. Inhibiting Islet Amyloid Polypeptide Fibril Formation by the Red Wine Compound Resveratrol. Chembiochem 10:445-+.
16. Radovan, D., N. Opitz, and R. Winter. 2009. Fluorescence microscopy studies on islet amyloid polypeptide fibrillation at heterogeneous and cellular membrane interfaces and its inhibition by resveratrol. Febs Letters 583:1439-1445.
17. Burgevin, M. C., M. Passat, N. Daniel, M. Capet, and A. Doble. 1994. CONGO-RED PROTECTS AGAINST TOXICITY OF BETA-AMYLOID PEPTIDES ON RAT HIPPOCAMPAL-NEURONS. Neuroreport 5:2429-2432.
18. Porat, Y., Y. Mazor, S. Efrat, and E. Gazit. 2004. Inhibition of islet amyloid polypeptide fibril formation: A potential role for heteroaromatic interactions. Biochemistry 43:14454-14462.
19. Tomiyama, T., H. Kaneko, K. Kataoka, S. Asano, and N. Endo. 1997. Rifampicin inhibits the toxicity of pre-aggregated amyloid peptides by binding to peptide fibrils and preventing amyloid-cell interaction. Biochemical Journal 322:859-865.
20. Harroun, T. A., J. P. Bradshaw, and R. H. Ashley. 2001. Inhibitors can arrest the membrane activity of human islet amyloid polypeptide independently of amyloid formation. Febs Letters 507:200-204.
21. Mishra, R., B. Bulic, D. Sellin, S. Jha, H. Waldmann, and R. Winter. 2008. Small-molecule inhibitors of islet amyloid polypeptide fibril formation. Angewandte Chemie-International Edition 47:4679-4682.
22. Liu, R., H. Barkhordarian, S. Emadi, C. B. Park, and M. R. Sierks. 2005. Trehalose differentially inhibits aggregation and neurotoxicity of beta-amyloid 40 and 42. Neurobiology of Disease 20:74-81.
23. Miura, Y., C. You, and R. Ohnishi. 2008. Inhibition of Alzheimer amyloid beta aggregation by polyvalent trehalose. Science and Technology of Advanced Materials 9.
24. Arora, A., C. Ha, and C. B. Park. 2004. Inhibition of insulin amyloid formation by small stress molecules. Febs Letters 564:121-125.
25. Tanaka, M., Y. Machida, S. Y. Niu, T. Ikeda, N. R. Jana, H. Doi, M. Kurosawa, M. Nekooki, and N. Nukina. 2004. Trehalose alleviates polyglutamine-mediated pathology in a mouse model of Huntington disease. Nature Medicine 10:148-154.
26. Doxastakis, M., A. K. Sum, and J. J. de Pablo. 2005. Modulating membrane properties: The effect of trehalose and cholesterol on a phospholipid bilayer. Journal of Physical Chemistry B 109:24173-24181.
27. Ohtake, S., C. Schebor, S. P. Palecek, and J. J. de Pablo. 2005. Phase behavior of freeze-dried phospholipid-cholesterol mixtures stabilized with trehalose. Biochimica Et Biophysica Acta-Biomembranes 1713:57-64.
28. Ricker, J. V., N. M. Tsvetkova, W. F. Wolkers, C. Leidy, F. Tablin, M. Longo, and J. H. Crowe. 2003. Trehalose maintains phase separation in an air-dried binary lipid mixture. Biophysical Journal 84:3045-3051.
29. Sugita, Y., and Y. Okamoto. 1999. Replica-exchange molecular dynamics method for protein folding. Chemical Physics Letters 314:141-151.

30. Liu, P., B. Kim, R. A. Friesner, and B. J. Berne. 2005. Replica exchange with solute tempering: A method for sampling biological systems in explicit water. Proceedings of the National Academy of Sciences of the United States of America 102:13749-13754.
31. Piana, S., K. Lindorff-Larsen, and D. E. Shaw. 2011. How Robust Are Protein Folding Simulations with Respect to Force Field Parameterization? Biophysical Journal 100:L47-L49.
32. Tieleman, D. P., and H. J. C. Berendsen. 1996. Molecular dynamics simulations of a fully hydrated dipalmitoyl phosphatidylcholine bilayer with different macroscopic boundary conditions and parameters. Journal of Chemical Physics 105:4871-4880.
33. Bussi, G., D. Donadio, and M. Parrinello. 2007. Canonical sampling through velocity rescaling. Journal of Chemical Physics 126:7.
34. Essmann, U., L. Perera, M. L. Berkowitz, T. Darden, H. Lee, and L. G. Pedersen. 1995. A SMOOTH PARTICLE MESH EWALD METHOD. Journal of Chemical Physics 103:8577-8593.
35. Hess, B., C. Kutzner, D. van der Spoel, and E. Lindahl. 2008. GROMACS 4: Algorithms for highly efficient, load-balanced, and scalable molecular simulation. Journal of Chemical Theory and Computation 4:435-447.
36. Kandt, C., W. L. Ash, and D. P. Tieleman. 2007. Setting up and running molecular dynamics simulations of membrane proteins. Methods 41:475-488.
37. Minones, J., P. Dynarowicz-Latka, J. M. R. Patino, and E. Iribarnegaray. 2003. Orientational changes in dipalmitoyl phosphatidyl glycerol Langmuir monolayers. Journal of Colloid and Interface Science 265:380-385.
38. Izmitli, A., C. Schebor, M. P. McGovern, A. S. Reddy, N. L. Abbott, and J. J. de Pablo. 2011. Effect of trehalose on the interaction of Alzheimer's A beta-peptide and anionic lipid monolayers. Biochimica Et Biophysica Acta-Biomembranes 1808:26-33.
39. Takamoto, D. Y., M. M. Lipp, A. von Nahmen, K. Y. C. Lee, A. J. Waring, and J. A. Zasadzinski. 2001. Interaction of lung surfactant proteins with anionic phospholipids. Biophysical Journal 81:153-169.
40. Lambruschini, C., A. Relini, A. Ridi, L. Cordone, and A. Gliozzi. 2000. Trehalose interacts with phospholipid polar heads in Langmuir monolayers. Langmuir 16:5467-5470.
41. Munoz, M., P. Sospedra, M. J. Gomara, C. Mestres, and I. Haro. 2004. The covalent coupling of HAV-VP3 (110-121) synthetic peptide to liposomes: physicochemical studies. International Journal of Pharmaceutics 269:177-184.
42. Sospedra, P., M. Espina, M. A. Alsina, I. Haro, and C. Mestres. 2001. Study at the air/water interface of a hepatitis A N-acetylated and C-amidated synthetic peptide (AcVP3(110-121)-NH2) - I. Surface activity and insertion in lipid monolayers. Journal of Colloid and Interface Science 244:79-86.
43. Engel, M. F. M., H. Yigittop, R. C. Elgersma, D. T. S. Rijkers, R. M. J. Liskamp, B. de Kruijff, J. W. M. Hoppener, and J. A. Killian. 2006. Islet amyloid polypeptide inserts into phospholipid monolayers as monomer. Journal of Molecular Biology 356:783-789.

44. Lopes, D. H. J., A. Meister, A. Gohlke, A. Hauser, A. Blume, and R. Winter. 2007. Mechanism of islet amyloid polypeptide fibrillation at lipid interfaces studied by infrared reflection absorption spectroscopy. Biophysical Journal 93:3132-3141.
45. Ege, C., and K. Y. C. Lee. 2004. Insertion of Alzheimer's A beta 40 peptide into lipid monolayers. Biophysical Journal 87:1732-1740.
46. Levine, H. 1993. THIOFLAVINE-T INTERACTION WITH SYNTHETIC ALZHEIMERS-DISEASE BETA-AMYLOID PEPTIDES - DETECTION OF AMYLOID AGGREGATION IN SOLUTION. Protein Science 2:404-410.
47. Domanov, Y. A., and P. K. J. Kinnunen. 2008. Islet amyloid polypeptide forms rigid lipid-protein amyloid fibrils on supported phospholipid bilayers. Journal of Molecular Biology 376:42-54.
48. Hebda, J. A., and A. D. Miranker. 2009. The Interplay of Catalysis and Toxicity by Amyloid Intermediates on Lipid Bilayers: Insights from Type II Diabetes. Annual Review of Biophysics 38:125-152.
49. Abedini, A., and D. P. Raleigh. 2005. The role of His-18 in amyloid formation by human islet amyloid polypeptide. Biochemistry 44:16284-16291.
50. Doxastakis, M., V. G. Sakai, S. Ohtake, J. K. Maranas, and J. J. de Pablo. 2007. A molecular view of melting in anhydrous phospholipidic membranes. Biophysical Journal 92:147-161.
51. Arakawa, T., and S. N. Timasheff. 1982. STABILIZATION OF PROTEIN-STRUCTURE BY SUGARS. Biochemistry 21:6536-6544.
52. Xie, G. F., and S. N. Timasheff. 1997. The thermodynamic mechanism of protein stabilization by trehalose. Biophysical Chemistry 64:25-43.

Conclusions

We have presented an improvement to the metadynamics algorithm that fully corrects boundary errors, while also being slightly faster for many systems. It allows the metadynamics to be generalized to any set of bounded collective variables.

We have seen that simulations that calculate the free energy simultaneously as a function of separation distance and an angle parameter can distinguish β-peptides with strong orientational preferences which are likely candidates to self-assemble into higher order structures from those with weak preferences that are unlikely to do so.

Finally, we examined the effect of trehalose on the interaction of hIAPP with DPPG monolayers. Using simulations, we showed that trehalose promotes α-helicity of monomers in bulk solution, but not at the membrane interface. Experiments showed that the formation of oligomers through α-helical intermediates at the membrane was promoted by trehalose. This suggests that the formation of α-helical secondary structures at the membrane interface is a cooperative process involving multiple peptides, that despite many similarities between diseases caused by protein aggregation, the effect of threhalose varies between them, and that solvent environments that promote α-helicity would not be appropriate for therapeutic applications.

Appendix A1: Experimental Methods for hIAPP System

Materials. Dimethyl sulfoxide (DMSO, 99.9%) and Thioflavin T (ThT) were obtained from Sigma-Aldrich (Milwaukee, WI). l,2-Dipalmitoyl-sn-Glycero-3-[Phospho-rac-1-glycerol)] (sodium salt) (DPPG) and dyed lipid, 1,2-Dipalmitoyl-sn-Glycero-3-Phosphoethanolamine-N-(7-nitro-2-1,3-benzoxadiazol-4-yl) (Ammonium salt) (NBD-PE) were obtained as solutions in chloroform from Avanti Polar Lipids Inc. (Alabaster, AL). Synthetic wild-type human (h-IAPP) was obtained from Bachem (King of Prussia, PA). Trehalose was purchased from Ferro Pfanstiehl Laboratories (Waukegan, IL). PBS: phosphate buffered saline solution pH 7.4 (11.9 mM Phosphates, 137 mM Sodium Chloride, 2.7 mM Potassium Chloride) was obtained from Fisher BioReagents (Fair Lawn, NJ).

Preparation of peptide stock solutions. Lyophilized hIAPP peptide from Bachem was dissolved in DMSO to obtain clear solutions. After 2 hours the peptide solution was sonicated in a bath sonicator for 1.5 min. Stock solutions in DMSO were stored at room temperature and used within two days.

Preparation of large unilamellar vesicles (LUV). Chloroform from DPPG aliquots was evaporated under a stream of nitrogen and dried in a vacuum desiccator overnight. The dried lipids were rehydrated at a temperature above the phase transition temperature (55°C) in a solution containing water, PBS buffer or 50mM calcein solution (for leakage experiments). The samples were then extruded through membrane filters (100nm pore diameter) 19 times using an extruder (Avanti polar lipids, Alabaster, AL) at 55°C. For leakage experiments, the calcein filled vesicles were separated from the free dye by size exclusion chromatography.

ThT fluorescence assay. Fibrillization of IAPP was monitored using the fluorescence intensity increase for ThT. The reaction mixture consisted of: ThT to yield a 50 µM solution (from a 5 mM stock solution in deionized distilled water), DPPG liposomes to yield a 100 µM solution, peptide (from a 1 mg/mL Stock solution in DMSO) to yield a 10 µM solution and either water, 100mM trehalose solution, PBS or 100 mM trehalose solution in PBS. The final concentration of DMSO in the reaction mixture was 2%. These low concentrations of DMSO have little effect on phospholipid membrane structure. Thioflavin T itself has been shown not to inhibit amyloid fiber formation of IAPP. Real-time emission intensities were measured at 482 nm with excitation at 450 nm. Measurements were performed at 30°C with excitation and emission slit widths of 1 nm, respectively, and an integration time of 0.4 seconds. Fluorescence measurements were taken using a Fluoromax-3 spectrofluorometer, Jobin Yvon (Edison, NJ).

Liposome leakage assay

Leakage assays were performed at a peptide concentration of 5 µM in plastic microcuvettes (reaction volume 500 µL) without stirring, by using a fluorometer at excitation and emission wavelengths of 491 and 520 nm, respectively, and excitation and emission band pass of 1 nm. The leakage experiments were started by adding calcein loaded liposomes to a mixture containing hIAPP and PBS or PBS/100 mM trehalose at 30 ± 1°C. The maximum leakage at the end of each experiment was determined by adding 10% Triton X-100 to a final concentration of 0.4%. The leakage fraction was calculated according to Equation (1): $L(t) = (F_t - F_0)/ (F_{100} - F_0)$, (1) where L(t) is the fraction of dye released, F(t) is the measured fluorescence intensity, and F_0 and F_{100} are the fluorescence intensities at time= 0 and after the addition of Triton X-100, respectively.

DPPG monolayer compression isotherms Compression isotherms were measured on a Nima 602A film balance (Coventry, England) equipped with a filter paper Wilhelmy plate for surface pressure measurements. Using a water bath, the temperature of the trough was kept at 30°C for all experiments. The compression isotherms were obtained by spreading a 1mg/ml DPPG solution in chloroform on the corresponding subphase (water, 100mM trehalose, PBS or PBS with 100mM trehalose), waiting for 20 minutes for chloroform to evaporate and finally compressing the monolayer at 35cm^2/min until collapse.

Constant pressure insertion experiments The constant surface pressure experiments were carried out in a computer-controlled Langmuir Teflon-coated trough (KSV Minimicro System 1S, Helsinki, Finland). The surface pressure was measured through a Wilhelmy-plate method using a roughened platinum plate connected to a microelectronic feedback system. The trough filled up with the corresponding solution (water, 100mM trehalose, PBS or PBS with 100mM trehalose) was thermostated using a water circulating bath. Monolayers were prepared by spreading the lipid solution on the aqueous subphase using a Hamilton syringe. An equilibration time of 20 min was allowed before compressing the monolayer at a rate of 5 mm/min. A constant surface pressure assay was used to monitor the insertion of the hIAPP peptide into DPPG monolayers. Constant-pressure assays were performed by spreading DPPG onto a subphase free of peptide, and then compressing the lipid film to the predetermined surface pressure (25 mN/m). Once the desired surface pressure was attained it was kept constant. A quantity of 45 μl out of a of 1 mg/ml hIAPP in DMSO solution was then aliquoted, topped off With 0.2 the corresponding buffer, and immediately injected into the subphase (50 ml) through an injection port using a syringe (Hamilton, Reno, NV). After peptide injection, the area was recorded as a function of time. In this constant-pressure mode, insertion of the peptide into the lipid led to an increase in the lipid surface area.

Fluorescence microscopy An inverted Olympus IX71 optical microscope was used to monitor the surface morphology of the monolayer. For this purpose, the trough was positioned above the microscope stage, placing the quartz window at the bottom of the trough over the microscope objective. A mercury lamp was used for the fluorescence excitation. A dichroic mirror/filter cube was employed to direct the light onto the monolayer and to filter the emitted fluorescence. Images were collected using a Hamamatsu ORCA-ER camera, Minneapolis, MN.

All reported experimental trends have been reproduced in at least three, completely independent experiments with different peptide stocks.